



LAWRENCE  
LIVERMORE  
NATIONAL  
LABORATORY

# Phase-field Modeling of Displacive Phase Transformations in Elastically Anisotropic and Inhomogeneous Polycrystals

T. W. Heo, L. Q. Chen

March 6, 2014

Acta Materialia

## **Disclaimer**

---

This document was prepared as an account of work sponsored by an agency of the United States government. Neither the United States government nor Lawrence Livermore National Security, LLC, nor any of their employees makes any warranty, expressed or implied, or assumes any legal liability or responsibility for the accuracy, completeness, or usefulness of any information, apparatus, product, or process disclosed, or represents that its use would not infringe privately owned rights. Reference herein to any specific commercial product, process, or service by trade name, trademark, manufacturer, or otherwise does not necessarily constitute or imply its endorsement, recommendation, or favoring by the United States government or Lawrence Livermore National Security, LLC. The views and opinions of authors expressed herein do not necessarily state or reflect those of the United States government or Lawrence Livermore National Security, LLC, and shall not be used for advertising or product endorsement purposes.

# Phase-field Modeling of Displacive Phase Transformations in Elastically Anisotropic and Inhomogeneous Polycrystals

Tae Wook Heo<sup>1,\*</sup> and Long-Qing Chen<sup>2</sup>

<sup>1</sup>*Condensed Matter and Materials Division, Lawrence Livermore National Laboratory, Livermore, CA 94550, USA*

<sup>2</sup>*Department of Materials Science and Engineering, The Pennsylvania State University, University Park, PA 16802, USA*

## Abstract

We integrate the inhomogeneous elasticity model and the phase-field equations for displacive phase transformations in polycrystalline materials. The relaxation of the misfit strain between parent and transformed product phases or among different structural variants of transformed product phases near grain boundaries is taken into account. It is applied to the *fcc* to *bcc* martensitic transformation described by a Bain strain in a polycrystalline Fe-31at.%Ni metallic alloy. The focus is on the effect of grain boundaries on the displacive transformation behaviors. We first study nucleation of the *bcc* product phase at a grain boundary of a bicrystal. The predicted microstructures through nucleation near grain boundaries are compared to existing experimental observations in literature. The effects of grain boundary characteristics such as the degree and range of the misfit strain relaxation at the grain boundary and grain boundary curvature on the phase behaviors near a grain boundary are then examined for both a flat or a curved grain boundary. The model is also applied to polycrystals containing multiple grains. The effects of the misfit strain relaxation at grain boundaries, elastic anisotropy, and applied stress on the kinetics and the microstructures of displacive transformations are discussed.

Keywords: Displacive phase transformation; Inhomogeneous elasticity; Elastic anisotropy; Polycrystals; Phase-field model

\*E-mail address: heo1@llnl.gov, htw584@gmail.com

Release #: LLNL-JRNL-651372

## 1. Introduction

Displacive phase transformations are common in a wide spectrum of materials ranging from metals to ceramics when a system is subject to temperature variation and/or mechanical deformation [1-6]. In many cases, a displacive transformation involves a change in crystal symmetry. Examples include the *bcc* to *hcp* transformation in titanium alloys [7], the *fcc* to *bcc* Bain transformation in steels [3], and the *hcp* to *fcc* structural change during hydride formation in zirconium alloys [8], to name just a few. A displacive transformation is accomplished by an atomic or crystal lattice rearrangement, *i.e.*, atomic shuffle and/or lattice distortion [1], driven by the chemical free energy reduction, resulting in multiple crystallographically equivalent structural variants of the product phase. The accommodation of lattice misfit between the structural variant and the parent phase or among domains of different orientations generates a significant amount of strain energy, and the relaxation of strain energy leads to complex self-assembling domain microstructures.

Structural defects such as dislocations, grain boundaries, precipitates or inclusions, free surfaces, *etc.* often play significant roles in the displacive transformation behavior by modifying the nucleation or kinetic barriers. In particular, grain boundaries in polycrystals can act as heterogeneous nucleation sites. Although there have been efforts to elucidate the effects of grain boundaries [9-11], it is still extremely challenging to experimentally capture the phase transformation kinetics and microstructural features during displacive structural changes since the transformations are very rapid and they produce complex microstructures. In addition, the presence of structural defects adds complexity to the transformation behaviors. Hence, there have been a number of theoretical and/or computational efforts [12-19] to uncover the underlying mechanisms and physics of displacive phase transformations. Phase-field method [20-25] based on the diffuse-interface description [26] has been successfully developed and employed to tackle the problems related to the displacive transformations [2]. The first successful three-dimensional phase-field model for the martensitic transformation, one type of displacive phase transformations [1], was proposed by Wang and Khachaturyan [27]. The model was developed for modeling the improper martensitic transformation and successfully employed to produce microstructural features during the nucleation, growth, and coarsening of the martensitic phase in the parent phase of a single crystalline metallic alloy. A phase-field model for a proper

martensitic transformation was also proposed [28]. A similar modeling framework has been adopted for modeling several types of crystal symmetry changes with or without diffusional processes [29-36]. Recently, the elasto-plastic effects have been incorporated to phase-field modeling of martensitic transformations by incorporating the dislocation dynamics [37, 38], and the elasto-plastic phase-field model [39] was applied to simulating the martensitic transformations by introducing a local plastic yielding criterion [40-45]. In addition, a vector model based on the phase-field theory for the proper displacive phase transformations has also been proposed to take into consideration the structural anisotropy and directional flexibility [46]. The phase-field models for martensitic transformations have been extended to study the transformation behaviors near structural defects such as dislocations [47], precipitates [48], free surfaces [49], void, stress-concentration sites, and inert inclusions [50], and to study the transformation behaviors in a thin film constrained by a substrate [51, 52] or in a multilayer system consisting of alternating active and inert layers [53]. General reviews of phase-field models for the martensitic transformation are available in [54, 55]. They have been also extended to model microstructure evolution during martensitic transformations in polycrystals [45, 56-60]. These models captured the essential features of the phase behavior in the presence of multiple grains. However, some details of the microscopic features near grain boundaries, *e.g.*, heterogeneous nucleation of variants near grain boundaries, were not analyzed. In existing phase-field simulations, pre-existing nuclei inside a grain were employed in most of the simulations in the absence of external loading, or external loading was applied to trigger the transformation inside grains or near grain boundaries [59]. In addition, all existing models are based on the isotropic homogeneous elasticity approximation although the models take into account the rotation of the transformation strain associated with the crystallographic orientation variation from one grain to another. Finally, existing models also ignore the possible misfit strain relaxation or loss near a grain boundary.

In this paper, we describe phase-field kinetic equations describing displacive phase transformations [61, 62] in elastically inhomogeneous and anisotropic polycrystals. In particular, the possible misfit strain relaxation or coherency loss at the grain boundaries is incorporated to capture the microscopic phase behaviors near the grain boundaries. The martensitic transformation in Fe-31at.%Ni alloy is employed as an example to study the generic features of the displacive transformation [1]. It will be the basis for our phase-field modeling of the phase

transformations and coupled microstructure evolution in polycrystalline alloys where both diffusional and displacive transformations take place.

## 2. Phase-field modeling

During a displacive structural transformation, multiple variants of the product phase are produced. The number of possible variants is determined by the symmetry of the crystal lattice rearrangement [17, 27]. For example, the *fcc* to *bcc* Bain transformation produces three crystallographically equivalent variants due to the tetragonal symmetry of the transformation strain, *i.e.*, the tetragonal axis of the strain can be aligned with any one of the three crystallographic directions [100], [010], and [001] in a cubic lattice. Therefore, multiple structural order parameters are required accordingly in order to account for the structural change within the phase-field context. In addition, for polycrystals, each grain contains its own set of structural order parameters [57]. Hence, we define the structural order parameter (or phase-field)  $\eta_{pg}(\vec{r}, t)$  where  $p$  represents the structural variant index and  $g$  represents the grain index in order to identify multiple structural variants in each grain. For instance,  $p=1, 2, 3$  and  $g=1, 2, \dots, N$  for the *fcc* to *bcc* Bain transformations in a polycrystal containing  $N$  grains. Recently, Malik *et al.* employed continuous structural order parameters across a grain boundary and they regarded a grain boundary as a kinetically frozen phase, acting as a kinetic barrier at the grain boundary, by varying the kinetic coefficient of the governing equation to account for the discontinuity of the transformation process across the grain boundary [59, 60]. It should be noted that our definition automatically takes into account the discontinuity of the structural order parameter across the grain boundary without specific considerations at the grain boundary without the significant loss of computational efficiency (See section 2.3 and Supplementary Material S1). The total free energy functional of the entire system is expressed as the following volume integral [27, 57]:

$$F = \int_V \left\{ f(\{\eta_{pg}\}) + \sum_g \sum_i \sum_j \sum_p \frac{\kappa_{p,ij,g}}{2} \nabla_i \eta_{pg} \nabla_j \eta_{pg} + e_{\text{coh}} \right\} d^3\vec{r}, \quad (1)$$

where  $\{\eta_{pg}\}$  is a set of structural order parameters,  $\kappa_{p,ij,g}$  is the gradient energy coefficient,  $i$  and  $j$  are indices of Cartesian coordinates, and  $e_{\text{coh}}$  is the coherency strain energy. We assign different gradient energy coefficient tensors for different grains following Ref. [57], and  $p$

represents the structural variant index and  $g$  represents the grain index in the definition of  $\kappa_{p,ij,g}$ . Following sections provide the details for various contributions to Eq. (1) using the  $fcc$  to  $bcc$  martensitic transformation as a representative example.

## 2.1. Chemical free energy

The thermodynamic driving force for the displacive phase transformation is the chemical free energy reduction. Therefore, it should be modeled in a way that the relevant thermodynamic or physical variables such as undercooling ( $\Delta T = T_0 - T$  where  $T$  is the undercooling temperature and  $T_0$  is the stress-free equilibrium temperature) and latent heat for the transformation ( $Q$ ) are properly reflected. The usual Landau-type free energy [27, 28, 47, 49, 53, 56, 57] for the local free energy density has the following form:

$$f(\{\eta_{pg}\}) = A_2 \sum_{p,g} \eta_{pg}^2 + A_3 \sum_{p,g} \eta_{pg}^3 + A_4 \sum_{p,g} \eta_{pg}^4 + A_{42} \sum_{p,g} \sum_{p',g'} \eta_{pg}^2 \eta_{p'g'}^2, \quad (2)$$

where  $A_2$ ,  $A_3$ ,  $A_4$ , and  $A_{42}$  are the Landau coefficients. However, this type of the function is not flexible to explicitly control the thermodynamic or physical variables. For example, the Landau coefficients were usually obtained by fitting the function to the free energy database for different materials [47]. Therefore, we utilized a different type of free energy function that explicitly incorporates temperature and latent heat for the transformation. The specific form the function is given by

$$\begin{aligned} f(\{\eta_{pg}\}, T) &= g(\{\eta_{pg}\}) + \Delta f^M(T) \cdot H(\{\eta_{pg}\}) \\ &= g(\{\eta_{pg}\}) + \frac{Q \cdot (T - T_0)}{T_0} \cdot H(\{\eta_{pg}\}), \end{aligned} \quad (3)$$

where the first term,  $g(\{\eta_{pg}\})$ , is the local stress-free chemical free energy at  $T = T_0$  and given by

$$g(\{\eta_{pg}\}) = a_0 \sum_{p,g} \eta_{pg}^2 (\eta_{pg} - 1)^2 + a_1 \sum_{p,g} \sum_{p',g'} \eta_{pg}^2 \eta_{p'g'}^2, \quad \text{and the second term, } \Delta f^M(T) \cdot H(\{\eta_{pg}\}),$$

represents the variation of the free energy due to undercooling with respect to  $T_0$  with  $H(\{\eta_{pg}\}) = \sum_{p,g} (-2\eta_{pg}^3 + 3\eta_{pg}^2)$ . The schematic plot of the local free energy as a function of a

single order parameter is shown in Fig. 1(a). It should be noted that the local free energy function without interaction terms in Eq. (3) recovers the 2-3-4 potential in Eq. (2) as the following:

$$f(\{\eta_{pg}\}, T) = \left[ a_0 + \frac{3Q \cdot (T - T_0)}{T_0} \right] \cdot \sum_{p,g} \eta_{pg}^2 - \left[ 2a_0 + \frac{2Q \cdot (T - T_0)}{T_0} \right] \cdot \sum_{p,g} \eta_{pg}^3 + a_0 \sum_{p,g} \eta_{pg}^4, \quad (4)$$

The free energy function has the following properties: (i)  $f(0, T) = 0$ , (ii)

$$f(1, T) = \frac{Q \cdot (T - T_0)}{T_0} < 0, \text{ (iii) } \left. \frac{\partial f(\eta, T)}{\partial \eta} \right|_{\eta=0,1} = 0. \text{ The property (iii) ensures that the equilibrium}$$

values for the order parameters are 0 or 1.

## 2.2. Coherency strain energy

The coherency strain energy stemming from the lattice mismatch is one of the major contributions to the thermodynamics and kinetics of phase transformations and the morphology of the microstructures during displacive phase transformations. The coherency strain energy density ( $e_{coh}$ ) in Eq. (1) is given by  $e_{coh} = \frac{1}{2} C_{ijkl} \varepsilon_{ij}^{el} \varepsilon_{kl}^{el}$  where  $\varepsilon_{ij}^{el}$  is the elastic strain tensor and  $C_{ijkl}$  is the elastic modulus. In polycrystals, the elastic modulus is always inhomogeneous since it contains grains of different crystallographic orientations. To model the position-dependent inhomogeneous elastic modulus of a polycrystal, the following mathematical expression is employed [61, 62]:

$$C_{ijkl}(\vec{r}) = \sum_g \theta_g(\vec{r}) a_{im}^g a_{jn}^g a_{ko}^g a_{lp}^g C_{mnop}^{ref}, \quad (5)$$

where  $\theta_g(\vec{r})$  is the grain shape function which is equal to 1 within the  $g$ th grain and equal to 0 outside,  $a_{ij}^g$  are the components of an axis transformation matrix for the rotation from the local coordinate system defined on the given  $g$ th grain to the global reference coordinate system, and  $C_{mnop}^{ref}$  is the elastic modulus of a grain in the local coordinate system. The rotation (or orientation) of the  $g$ th grain is represented by  $\alpha_g$ , in two-dimensional (2D) systems, with

$$[a_{ij}^g] = \begin{pmatrix} \cos \alpha_g & \sin \alpha_g \\ -\sin \alpha_g & \cos \alpha_g \end{pmatrix} \quad (6-1)$$

or the Euler angles  $\alpha_g$ ,  $\beta_g$ , and  $\gamma_g$ , in three-dimensional (3D) systems, with



$$[a_{ij}^g] = \begin{pmatrix} \cos \alpha_g \cos \beta_g - \sin \alpha_g \sin \beta_g \cos \gamma_g & \sin \alpha_g \cos \beta_g + \cos \alpha_g \sin \beta_g \cos \gamma_g & \sin \beta_g \sin \gamma_g \\ -\cos \alpha_g \sin \beta_g - \sin \alpha_g \cos \beta_g \cos \gamma_g & -\sin \alpha_g \sin \beta_g + \cos \alpha_g \cos \beta_g \cos \gamma_g & \cos \beta_g \sin \gamma_g \\ \sin \alpha_g \sin \gamma_g & -\cos \alpha_g \sin \gamma_g & \cos \gamma_g \end{pmatrix}. \quad (6-2)$$

In principle, the elastic modulus of the variants can be distinguished from the parent phase by expressing  $C_{mnop}^{\text{ref}}$  as, for example,  $C_{mnop}^{\text{ref}} = H(\{\eta_{pg}\})C_{mnop}^{\text{ref,V}} + (1 - H(\{\eta_{pg}\}))C_{mnop}^{\text{ref,P}}$  where  $C_{mnop}^{\text{ref,V}}$  and  $C_{mnop}^{\text{ref,P}}$  are the elastic moduli of the variants and the parent phase, respectively [36]. However, we assume that the elastic modulus of a grain interior is homogeneous since the difference in the elastic modulus between *fcc* and *bcc* structures caused by such a small lattice distortion would not be significant, and we therefore only consider the elastic inhomogeneity caused by the different crystallographic orientations of grains in a polycrystal.

Following Khachaturyan's microelasticity theory [2], the elastic strain is expressed by the homogeneous strain ( $\bar{\varepsilon}_{ij}$ ), the heterogeneous strain ( $\delta\varepsilon_{ij}$ ), and the eigenstrain ( $\varepsilon_{ij}^0$ ):  $\varepsilon_{ij}^{el}(\vec{r}) = \bar{\varepsilon}_{ij} + \delta\varepsilon_{ij}(\vec{r}) - \varepsilon_{ij}^0(\vec{r})$ . The coherency during the displacive transformation is represented by the eigenstrain. The eigenstrain in a polycrystal is given by

$$\varepsilon_{ij}^0(\vec{r}) = \sum_g \theta_g(\vec{r}) \sum_p \varepsilon_{ij}^{00}(g, p, \vec{r}) \lambda(\eta_{pg}), \quad (7)$$

where  $\theta_g(\vec{r})$  is the grain shape function and  $\lambda(\eta_{pg})$  is the piecewise function of a structural order parameter which is given by

$$\begin{aligned} \lambda(\eta_{pg}) &= \eta_{pg} & (\text{when } \varepsilon < \eta_{pg} < 1 - \varepsilon) \\ &= -2\eta_{pg}^3 + 3\eta_{pg}^2 & (\text{when } \eta_{pg} < \varepsilon \text{ or } \eta_{pg} > 1 - \varepsilon), \end{aligned} \quad (8)$$

with a small value  $\varepsilon$ . During a transformation from the parent phase to the product phase,  $\eta_{pg}$  is used for  $\lambda(\eta_{pg})$  as in [56, 57]. However, the 3rd order polynomial is employed near the equilibrium states to avoid the unnecessary or unphysical artificial shift of the equilibrium values of the order parameter due to the coherency strain energy contribution.  $\varepsilon_{ij}^{00}(g, p, \vec{r})$  is the stress-free transformation strain in the polycrystal and is given by

$$\varepsilon_{ij}^{00}(g, p, \vec{r}) = \varphi(\vec{r}) a_{ik}^g a_{jl}^g \varepsilon_{kl}^{000}(p), \quad (9)$$

where  $a_{ij}^g$  are the components of an axis transformation matrix. In the case of the *fcc* to *bcc* transformation in Fe-31at.%Ni, the Bain strains with the tetragonal symmetry are employed for

$\varepsilon_{kl}^{000}(p)$ . The Bain strains can be easily derived from the crystallographic relationship between *fcc* and *bcc* structures. The *bcc* structure is established by the tetragonal distortion of the lattice represented by dashed lines in Fig. 2, leading to

$$[\varepsilon_{ij}^{000}(1)] = \begin{pmatrix} \varepsilon_3 & 0 & 0 \\ 0 & \varepsilon_1 & 0 \\ 0 & 0 & \varepsilon_1 \end{pmatrix}, [\varepsilon_{ij}^{000}(2)] = \begin{pmatrix} \varepsilon_1 & 0 & 0 \\ 0 & \varepsilon_3 & 0 \\ 0 & 0 & \varepsilon_1 \end{pmatrix}, [\varepsilon_{ij}^{000}(3)] = \begin{pmatrix} \varepsilon_1 & 0 & 0 \\ 0 & \varepsilon_1 & 0 \\ 0 & 0 & \varepsilon_3 \end{pmatrix}, \quad (10)$$

where  $\varepsilon_1 = (a_{bcc} - \frac{\sqrt{2}}{2}a_{fcc})/\frac{\sqrt{2}}{2}a_{fcc}$  and  $\varepsilon_3 = (a_{bcc} - a_{fcc})/a_{fcc}$  with lattice parameters of *fcc* ( $a_{fcc}$ ) and *bcc* ( $a_{bcc}$ ) structures. Due to the relatively disordered or opened structure of grain boundaries [63-65], the misfit strain can be mitigated near the grain boundary. In addition, the existence of solute atoms and/or dislocations at the grain boundary can alter the degree of misfit strain relaxation near the grain boundary by changing the local structure of the grain boundary [66, 67]. It should be mentioned that the misfit strain relaxation near the grain boundary may affect the metastability of the parent phase with respect to its displacive transformations, similar to other types of structural defects [47, 68]. In contrast to all existing phase-field models for displacive transformations, we employ the interpolation function ( $\varphi(\vec{r})$  in Eq. (9)) to consider the relaxation or partial loss of the misfit strain. The function has the following properties to model the misfit strain relaxation:  $\varphi(\vec{r})=1$  inside a grain and  $\varphi(\vec{r})<1$  near the center of a grain boundary. The explicit form of  $\varphi(\vec{r})$  in our model is given by

$$\varphi(\vec{r}) = \frac{[\rho(\phi_{\max} - \phi) + (\phi - \phi_{\min})]}{\phi_{\max} - \phi_{\min}}, \quad (11)$$

where  $\phi = \sum_g \xi_g^2$ ,  $\xi_g$  is the diffuse-interface grain order parameter (or phase-field) which is employed for generating a grain structure (the procedure for the grain structure generation is explained in section 3.1 and Supplementary Material S2), and  $\rho$  represents the misfit strain relaxation parameter associated with the degree of the relaxation at the center of the grain boundary, e.g.,  $\rho=1$ : no relaxation,  $\rho=0$ : full relaxation.

The macroscopic shape change of the system is represented by the homogeneous strain  $\bar{\varepsilon}_{ij}$ . The homogeneous strain is defined in such a way that  $\int_V \delta \varepsilon_{ij}(\vec{r}) dV = 0$ , which results in

$\bar{\varepsilon}_{ij} = \langle S_{ijkl} \rangle (\sigma_{ij}^a + \langle \sigma_{ij}^0 \rangle - \langle \delta \sigma_{ij} \rangle)$  where  $\langle S_{ijkl} \rangle = \langle C_{ijkl} \rangle^{-1}$ ,  $\langle C_{ijkl} \rangle = (1/V) \int_V C_{ijkl}(\vec{r}) dV$ ,  $\sigma_{ij}^a$  is an applied stress,  $\langle \sigma_{ij}^0 \rangle = (1/V) \int_V C_{ijkl}(\vec{r}) \varepsilon_{kl}^0(\vec{r}) dV$ , and  $\langle \delta \sigma_{ij} \rangle = (1/V) \int_V C_{ijkl}(\vec{r}) \delta \varepsilon_{kl}(\vec{r}) dV$  if the boundaries of the polycrystal are allowed to relax. When the system is subject to a constant applied strain ( $\varepsilon_{ij}^a$ ), the homogeneous strain is equal to the applied strain, *i.e.*,  $\bar{\varepsilon}_{ij} = \varepsilon_{ij}^a$  [61, 62].

The heterogeneous strain is expressed by the elastic displacement field  $u_i(\vec{r})$  as  $\delta \varepsilon_{ij}(\vec{r}) = (1/2)(\partial u_i / \partial r_j + \partial u_j / \partial r_i)$  [2]. The elastic solutions are obtained by solving the following mechanical equilibrium equation:

$$\nabla_j \sigma_{ij} = \nabla_j [C_{ijkl}(\vec{r}) \cdot (\bar{\varepsilon}_{kl} + \delta \varepsilon_{kl}(\vec{r}) - \varepsilon_{kl}^0(\vec{r}))] = 0, \quad (12)$$

where  $\sigma_{ij}$  is the local stress. The equation is solved by the Fourier-spectral iterative-perturbation method [69, 70]. The position-dependent elastic modulus in Eq. (5) splits into a constant homogeneous part  $C_{ijkl}^{\text{hom}}$  and a position-dependent inhomogeneous perturbation part  $C_{ijkl}^{\text{inhom}}(\vec{r})$ .

Therefore, Eq. (12) becomes

$C_{ijkl}^{\text{hom}}(\partial^2 u_k / \partial r_j \partial r_l) = \nabla_j [C_{ijkl}(\vec{r})(\varepsilon_{kl}^0 - \bar{\varepsilon}_{kl})] - \partial [C_{ijkl}^{\text{inhom}}(\vec{r})(\partial u_k / \partial r_l)] / \partial r_j$ . To obtain the accurate solution, the iterations are repeated until the value of

$\sqrt{\int_V [(u_1^{n+1} - u_1^n)^2 + (u_2^{n+1} - u_2^n)^2 + (u_3^{n+1} - u_3^n)^2] dV}$  becomes smaller than  $1.0 \times 10^{-4}$  for 2D

simulations or  $3.0 \times 10^{-4}$  for 3D simulations in this study. More details of the procedure can be found in our previous works [61, 62, 71].

### 2.3. Governing equation

The kinetics of structural phase transformation is governed by the Allen-Cahn (or time-dependent Ginzburg-Landau) equation. The governing equation for the structural order parameters in a single crystal [27] are modified to describe the evolutions of separately defined order parameters in different multiple grains [57]. The modified Allen-Cahn equation is given by [57]

$$\begin{aligned}
\frac{\partial \eta_{pg}(\vec{r}, t)}{\partial t} &= \theta_g(\vec{r}) \left[ -L \left( \frac{\delta F}{\delta \eta_{pg}} \right) + \zeta_g(\vec{r}, t) \right] \\
&= \theta_g(\vec{r}) \left[ -L \left( \frac{\partial f(\{\eta_{pg}\})}{\partial \eta_{pg}} - \kappa_{p,ij,g} \nabla_i \nabla_j \eta_{pg} + \frac{\partial e_{\text{coh}}}{\partial \eta_{pg}} \right) + \zeta_g(\vec{r}, t) \right]
\end{aligned} \tag{13}$$

where  $\theta_g(\vec{r})$  is the grain shape function,  $L$  is the kinetic coefficient, and  $\zeta_g(\vec{r}, t)$  is the Gaussian Langevin noise term. The use of the grain shape function  $\theta_g(\vec{r})$ , which is equal to 1.0 only within grain  $g$ , selectively allows the structural order parameters corresponding to that grain to evolve only within the particular grain  $g$ . It should be noted that their unnecessary evolution within other grains may result in unphysical interactions among order parameters. The modified equation is, however, numerically inefficient if the equation is solved in the Fourier space since all of  $g$  sets of order parameters ( $p \times g$  order parameters) at a position  $\vec{r}$  should be considered during the simulations, *i.e.*, each position contains a large number of order parameters to be solved. However, it should be noted that only one set of order parameters ( $p$  order parameters) is active or effective in a particular grain (grain index  $g'$ ). Therefore, only those order parameters should be considered in the particular grain for better efficiency. Solving the equation in the Fourier space does not allow to specify the active grain index  $g'$  at the position  $\vec{r}$  defined in a real space. Therefore, the numerical calculations are conducted in a real space using the simple Euler method in this study. The calculation in a real space allows us to select the active  $p$  order parameters (correspond to the active grain index  $g'$ ) participating in the evolution at the position  $\vec{r}$ . Thus, the equations for only active  $p$  order parameters are solved at the position  $\vec{r}$ , resulting in the reduction in the number of equations to be solved compared to solving equations in the Fourier space. For better accuracy, only the variational derivative of the gradient energy term ( $\kappa_{p,ij,g} \nabla_i \nabla_j \eta_{pg}$ ) is computed in the Fourier space.

### 3. Computer simulations and discussion

#### 3.1. Preparation of grain structures and simulation parameters

In this study, 2D bicrystal ( $512 \Delta x \times 256 \Delta y$ ), 3D bicrystal ( $256 \Delta x \times 128 \Delta y \times 128 \Delta z$ ), and 3D polycrystal ( $112 \Delta x \times 112 \Delta y \times 112 \Delta z$ ) are generated by a phase-field grain growth model [72, 73] (The details can be found in Supplementary Material S2) and utilized for the phase-field

simulations of displacive transformations, and the generated grain structures are shown in Fig. 3 where the monitor function is chosen to be  $\phi = \sum_g \xi_g^2$ . We employed uniform grids, *i.e.*,  $\Delta x = \Delta y = \Delta z$ . The information for the spatial distribution of grain order parameters is utilized to construct the interpolation function ( $\phi(\vec{r})$ ) for the misfit strain relaxation in Eq. (9) as explained above. It should be mentioned that the magnitude of the gradient energy coefficient determines how diffuse the grain order parameters are near the interface between adjoining grains, which is related to the grain boundary width in the context of phase-field grain growth model [72, 73]. In our model, the degree of diffuseness of grain order parameters determines the range of misfit strain relaxation from the center of grain boundaries by the definition of the interpolation function ( $\phi(\vec{r})$ ) for the misfit strain relaxation in Eq. (9). The grain shape function  $\theta_g(\vec{r})$  is also defined using the information of the spatial distribution grain order parameters ( $\xi_g$ ) in a way that  $\theta_g(\vec{r})$  is equal to 1 within the  $g$ th grain and equal to 0 outside the  $g$ th grain. Therefore, the grain shape function is obtained by comparing the magnitudes of grain order parameters at a given location and finding the grain index  $g$  of which corresponding grain order parameter has the maximum value. We performed computer simulations of displacive transformations on static grain structures assuming that a displacive transformation is much faster than the grain structure evolution at the simulation temperatures.

The physical parameters for simulations were chosen to be close to a Fe-31at.%Ni alloy as in [28, 47, 57]. The latent heat for the transformation and the stress-free equilibrium temperature were chosen to be  $Q = 3.5 \times 10^8 J/m^3$  [74] and  $T_0 = 405K$  [75, 76], respectively. The variation of free energy curve at different temperatures is presented in Fig. 1(b) in a non-dimensionalized form. The components of the Bain strain tensors were chosen to be  $\varepsilon_1 = 0.1322$  and  $\varepsilon_3 = -0.1994$  [77]. The coefficients  $a_0$  and  $\kappa_{p,ij,g}$  were chosen to produce an interfacial energy of  $\sim 99 mJ/m^2$ . We employed the isotropic interfacial energy for simplicity in this work although the model is able to account for the anisotropy. For the elastic modulus, we considered different cases of anisotropic elasticity with a fixed average shear modulus ( $\mu$ ) and average Poisson's ratio ( $\nu$ ):  $\mu = 28$  GPa and  $\nu = 0.375$  [47, 78] to investigate the effect of elastic anisotropy on the displacive transformation behavior near grain boundaries since the martensitic features are

determined by the ratio of the typical strain energy ( $\mu\varepsilon_0^2$ ) to the chemical driving force ( $|\Delta f|$ ) where  $\varepsilon_0$  is the typical stress-free transformation strain [17, 27]. Three independent components ( $C_{11}$ ,  $C_{12}$ ,  $C_{44}$  in the Voigt notation) of the elastic modulus of a cubic material are obtained for three different anisotropy cases ( $A_z=0.5, 1.0$ , and  $2.0$ ) of  $A_z$  ( $=2C_{44}/(C_{11}-C_{12})$ ) using the following formula [79]:

$$\begin{aligned} C_{11} &= \mu \left( \frac{2(2 + A_z)}{1 + A_z} - \frac{1 - 4\nu}{1 - 2\nu} \right), \\ C_{12} &= \mu \left( \frac{2A_z}{1 + A_z} - \frac{1 - 4\nu}{1 - 2\nu} \right), \\ C_{44} &= \mu \frac{2A_z}{1 + A_z}. \end{aligned} \quad (14)$$

The governing equation in Eq. (13) was solved in dimensionless forms. The physical parameters were non-dimensionalized by  $\Delta x^* = \frac{\Delta x}{l}$ ,  $\Delta t^* = L \cdot E \cdot \Delta t$ ,  $f^* = \frac{f}{E}$ ,  $g^* = \frac{g}{E}$ ,  $C_{ij}^* = \frac{C_{ij}}{E}$ , and  $\kappa^* = \frac{\kappa}{E \cdot l^2}$  where  $E$  is the characteristic energy which was chosen to be  $3.0788 \times 10^9 \text{ J/m}^3$  and  $l$  is the characteristic length which was taken to be  $0.8 \times 10^{-9} \text{ m}$ . The non-dimensionalized parameters are tabulated in Table 1.

### 3.2. Grain boundary nucleation mechanism

To examine the displacive transformation behavior near a grain boundary, we first employed a simple 2D *fcc* grain structure containing two grains, *i.e.*, a bicrystal in Fig. 3(a), separated by a flat grain boundary with elastic anisotropy  $A_z=2.0$  and the misfit strain relaxation parameter  $\rho=0.2$ . The temperature was chosen to be  $267\text{K}$  and the right-hand side grain was slightly rotated ( $\alpha_g = \pi/6$ ) with respect to the left-hand side grain. The random fluctuations of order parameters were incorporated at the initial stage. Fig. 4 shows the temporal evolution of *bcc* structural variants (order parameters) during the nucleation process. First of all, the simulations show the displacive transformations at grain boundaries without pre-existing nuclei in grain interior or external loading as shown in Fig. 4. It should be mentioned that the simulated microstructures in the figure are similar to the experimental observations [9, 10] of martensitic

transformation nucleated at grain boundaries. The nucleation occurs due to the lowered metastability of the parent (*fcc*) phase with respect to the product (*bcc*) phase at the grain boundary compared to the bulk counterpart since the nucleation barrier for the formation of *bcc* variants is reduced or vanishes due to the relaxation of misfit strain. One notable observation here is that the variants nucleated at grain boundaries do not propagate to the grain interior until two different variants meet together. Once two different variants merge or happen to nucleate close to each other, they grow into the grain interior together maintaining a twin-related structure. The orientation of the interface between two adjoining *bcc* variants is aligned to the invariant plane orientation. It can be understood that the formation of the twinned structure leads to lower strain energy by strain accommodation. A single variant sometimes nucleates and grows alone, but the self-nucleation of another variant subsequently occurs to reduce the strain energy as indicated by dashed circles at  $7500\Delta t$  and  $10000\Delta t$  in the figure. We also conducted a 3D computer simulation and confirmed that the nucleation of *bcc* variants occurs by the same mechanism (See Supplementary Material S3). In order to observe the nucleation behavior of *bcc* variants across a grain boundary, we carried out another 2D simulation starting with a pre-existing *bcc* particle in the left-hand side grain with initial small random fluctuations of order parameters (Fig. 5). The grain structure is the same as the 2D bicrystal above. The pre-existing *bcc* phase grows with self-nucleated variants and eventually encounters the grain boundary. As shown at  $700\Delta t$  in Fig. 5, the grain boundary nucleation occurs subsequently in the right-hand side grain and the nucleated *bcc* variant grows into the right-hand side grain as indicated by dashed circles, *i.e.*, our model correctly embodies the cooperative nucleation behavior [9, 10] of the displacive transformation across a grain boundary.

### 3.3. Effects of grain boundary characteristics on variant nucleation

We performed parametric simulations using a simple 3D bicrystal ( $256\Delta x \times 128\Delta y \times 128\Delta z$ ) to study the degree and range of the misfit strain relaxation and grain boundary curvature on displacive transformation behaviors and microstructure evolution. Depending on grain boundary types and properties, a grain boundary would exhibit different characteristics of misfit strain relaxation or coherency loss. In our model, the degree of relaxation is controlled by changing the parameter  $\rho$  in Eq. (11). To observe the nucleation behavior near a grain boundary with

changing  $\rho$  values, computer simulations were carried out for selected  $\rho$  values from 0.05 to 0.35 for a bicrystal with elastic anisotropy  $A_z=0.5$  containing a flat grain boundary. The temperature ( $T$ ) of the system was chosen to be 205K, and the Euler angles of the left-hand and right hand side grains were set to be (0,0,0) and ( $\pi/6$ ,0,0), respectively. Fig. 6 shows the temporal evolution for different  $\rho$  values. First of all, the nucleation of the *bcc* phase was observed for all the selected  $\rho$  values at  $2000\Delta t$  (Fig. 6). Interestingly, one particular *bcc* variant (variant 1) dominantly nucleates at the grain boundary when  $\rho$  is small ( $\rho=0.05$ ), but other variants (variant 2 and 3) also equally nucleate at the grain boundary when  $\rho$  is large ( $\rho=0.15,0.25$ ). In other words, only one variant tends to nucleate at a grain boundary when the misfit strain is more relaxed, but multiple *bcc* variants tend to nucleate at the grain boundary when the misfit strain is less relaxed. As a result, the nucleated *bcc* phase cannot grow into the grain interior and just forms a thick plate consisting of mostly one variant at the grain boundary when  $\rho=0.05$ . On the other hand, when  $\rho=0.25$ , the nucleated *bcc* phase grows into the grain while maintaining twin structures as shown in Fig. 6 following the nucleation and growth mechanism explained in section 3.2. It should be noted that very low nucleation density was observed in the case of  $\rho=0.35$  due to the lack of misfit strain relaxation compared to other cases. Therefore, we can conclude that there exists an optimal misfit strain relaxation for the fastest kinetics of displacive transformation nucleated at a flat grain boundary, and the kinetics can be engineered by adjusting the misfit strain relaxation at the grain boundary using, for example, the grain boundary segregation of solute atoms [80]. However, it should be mentioned that it is difficult to control the misfit strain experimentally.

The spatial distribution of  $\phi(\vec{r})$  in Eq. (11) determines the range of the misfit strain relaxation. The profile of  $\phi(\vec{r})$  can be controlled by the gradient energy coefficient ( $\kappa_g$ ) for grain order parameters in Eq. (S.1), and the profiles for three selected different values of  $\kappa_g$  with  $\rho=0.2$  are shown in Fig. 7(a). The temporal evolution of *bcc* phase formation near the grain boundary was studied for different cases of misfit strain relaxation range in a bicrystal ( $A_z=0.5$ ) containing a flat grain boundary with partial misfit strain relaxation ( $\rho=0.2$ ) (Fig. 7(b)). The temperature ( $T$ ) was chosen to be 205K, and the Euler angles of the left-hand and right hand side grains were (0,0,0) and ( $\pi/6$ ,0,0), respectively. When the relaxation range is narrow such as



$\kappa_g=1$ , the nucleation density of the *bcc* phase is so low that it cannot further grow. However, as the relaxation range becomes wider, the phase transformation occurs more rapidly. It is possible to nucleate more nuclei at or near the grain boundary since more volume near the grain boundary are initially occupied by the less stable *fcc* phase with respect to the displacive transformation in Fig. 7(a).

Another important characteristic of a grain boundary which possibly affects the displacive transformation behavior is its geometry. Grain boundaries in an actual grain structure usually display complex geometries, and they are interconnected to each other, forming the complex grain boundary network. For example, a grain boundary can be curved. To examine the impacts of grain boundary curvature on the displacive transformation, we also generated a simple bicrystal ( $A_z=0.5$ ). For comparison, three different types of curvatures were employed: flat, low curvature, and high curvature as shown in Fig. 8(a). We use the same  $\rho$  ( $=0.2$ ),  $\kappa_g$  ( $=3.0$ ), and temperature ( $=205K$ ) for the bicrystals with differently curved grain boundaries. The Euler angles of the left-hand and right-hand side grains were also set to be  $(0,0,0)$  and  $(\pi/6,0,0)$ , respectively. First of all, the behavior of the *bcc* phase formation at or near the grain boundary varies with the grain boundary curvature. More curved grain boundary promotes the phase transformations. The curved grain boundary seems to allow different types of *bcc* variants to nucleate simultaneously, and they, in turn, form a twinned structure which is prone to growth into the grain.

Interestingly, there seems to be a transition in the *bcc* phase domain structure near the curved grain boundaries (see the magnified view at  $5000\Delta t$  in Fig. 8(b)). The twinned structure consisting of variant 1 and 2 appears next to the curved grain boundary first as indicated by dashed circles in the figure, and then different twin structures consisting of mostly variant 2 and 3 tend to appear as observed near the flat grain boundary in Figs. 6 or 7. In other words, the optimal spatial configuration of *bcc* variants to minimize the strain energy is altered depending upon the distance from the curved grain boundary. It implies that grain boundary geometry has a strong effect on the spatial distribution of structural variants of displacive transformation.

### 3.4. Displacive transformation behavior in polycrystalline grain structures

Based on the understanding of phase behaviors in a bicrystal, we then studied the phase transformation behaviors in more realistic polycrystalline structures shown in Fig. 3(c). We investigated the impacts of strain relaxation at grain boundaries and an applied stress on displacive transformations in polycrystals. The Euler angles ( $\alpha_g, \beta_g, \gamma_g$ ) of grains were randomly assigned. The  $\kappa_g$  was set to be 3.0 for the polycrystals and temperature was chosen to be 202K.

#### **3.4.1. Effects of misfit strain relaxation at grain boundaries**

We first examined the transformation behaviors in a polycrystal with different degrees of misfit relaxation. We chose five different  $\rho$  values from 0.0 to 0.2 in Eq. (11) and three different elastic anisotropy ( $A_z=0.5, 1.0$ , and  $2.0$ ). Fig. 9(a) shows the microstructures at the later stage (at  $18000\Delta t$ ) for two selected  $\rho$  values (0.0 and 0.2) with different elastic anisotropy cases as an example. The temporal evolution of microstructures during a displacive transformation can be found in Supplementary Material S4. To quantify the overall kinetics, the total volume fractions ( $V_f$ ) of the *bcc* phase including all three variants (see Fig. 9 (b) to (d)) as well as the volume fraction of each variant (see Figs. S.2 and S.3 in Supplementary Material S4) were measured as a function of time. First of all, regardless of the elastic anisotropy, as  $\rho$  increases, *i.e.*, with less misfit strain relaxation, the overall kinetics becomes slow due to decreasing nucleation density at or near grain boundaries as shown in Figs. 9(b) to (d), S.2, and S.3. The volume fraction of each variant may be affected by the degree of the misfit strain relaxation (see Figs. S.2, and S.3), leading to different microstructures at the later stage with different  $\rho$  values as shown in Fig. 9(a). Contrary to the transformation behavior with different  $\rho$  values in a bicrystal explained above, all three variants nucleate near grain boundaries in polycrystals even when the misfit strain is highly or fully relaxed, *e.g.*,  $\rho=0.00$  in Fig. 9(a). The curvature might play a role in nucleating all the variants according to our simulation results of bicrystals with curved grain boundaries discussed above. As a result, the nucleated *bcc* phases grow into the grains and the phase transformation proceeds even when the misfit strain is fully relaxed in contrast to the case of the simple bicrystal containing the flat grain boundary.

For more analyses, the required time steps for achieving  $V_f=0.5$  which is denoted as  $\tau_{0.5}$  (as indicated in Fig. 9(b)) were plotted as a function of  $\rho$  in Fig. 9(e). Interestingly,  $\tau_{0.5}$  as a function of  $\rho$  displays a nonlinear characteristic in all three  $A_z$  cases as shown in the figure. One of the intriguing features for the overall kinetics is the difference in its sensitivity to the misfit strain relaxation under the three different elastic anisotropy. As clearly seen in Fig. 9(e),  $\tau_{0.5}$  for  $A_z=1.0$  is more sensitive to  $\rho$  than other two cases and the differences become large as  $\rho$  increases. The effects of elastic anisotropy become more significant as  $\rho$  increases, including its effects on the volume fraction of each variant and the spatial configuration of *bcc* variants. For example, when  $\rho=0.0$  in Fig. S.2, there are no significant differences in the volume fraction of each variant as a function of time and in the microstructure at the later stage, *e.g.*, at  $18000\Delta t^*$ , among 3 different cases of  $A_z$ . On the other hand, when  $\rho=0.2$  (see Fig. S.3), different cases of  $A_z$  display different characteristics in the temporal evolution of the volume fraction of each variant, and the microstructures at the later stage are also significantly different from each other.

The above results can be rationalized by the grain boundary nucleation density and the types of interfaces formed during nucleation and growth. During the growth process, two types of interfaces appear. One is the interface between parent *fcc* phase and product *bcc* phase (denoted as Type I hereafter), and the other is the twin boundary between *bcc* phases (denoted as Type II hereafter). Type I interface produces relatively high coherency strain energy. In addition, depending on the elastic anisotropy, the development of the coherency stress field arising from the lattice mismatch between parent *fcc* and product *bcc* phases might be different. To demonstrate the stress field development between the two phases during the variant growth, we designed simple simulations with a simple 2D bicrystal containing a single *bcc* variant embedded in a left-hand side *fcc* grain and monitored the evolution of the von Mises equivalent stress field ( $\sigma_{von}(\vec{r})$ ) defined by

$$\sigma_{von}(\vec{r}) = \sqrt{0.5[(\sigma_{xx} - \sigma_{yy})^2 + (\sigma_{yy} - \sigma_{zz})^2 + (\sigma_{xx} - \sigma_{zz})^2 + 6(\sigma_{xy}^2 + \sigma_{yz}^2 + \sigma_{xz}^2)]}. \quad (15)$$

Fig. 10(b) shows the stress profiles when the size of a growing *bcc* variant in the *fcc* phase are similar for different cases of  $A_z$  as shown in Fig. 10(a). As seen in Fig. 10(b), three different  $A_z$  cases display different equivalent stress profiles near the *bcc* variant. Moreover, we also confirmed that the growth speeds are different depending on the elastic anisotropy although it is

not clearly demonstrated in the figure. Since the long-range stress field may have significant effects on the kinetic pathways, different stress fields in Fig. 10(b) would result in different growth kinetics. Therefore, when Type I interfaces are dominant in a microstructure, the phase transformation behaviors can be strongly affected by the elastic anisotropy. On the other hand, Type II interface produces very low or almost zero coherency strain energy since the lattices between two *bcc* variants are compatible at the interface. Therefore, generated coherency strain energy is relatively less sensitive to the elasticity compared to that of Type I interface. As mentioned above, the nucleation density at or near grain boundaries decreases as  $\rho$  increases. When the grain boundary nucleation density is low, Type I interfaces are more likely to appear since most growing single *bcc* variants or twin-related structure unit are exposed to the *fcc* parent phase. Therefore, the kinetics and the resultant microstructures should be sensitive to the elastic anisotropy. However, when the grain boundary nucleation rate is high, dominant interfaces appearing during the growth are Type II interfaces as the case shown in Fig. 7 ( $\kappa_g=3.0$ ), leading to lower sensitivity to the elastic anisotropy. It should be noted that the elastic anisotropy does not have a strong effect on the grain boundary nucleation density at the early stage of the transformation, *e.g.*,  $1000\Delta t$  in Figs. S.2 and S.3. Therefore, the nucleation density is determined by the misfit strain relaxation regardless of elastic anisotropy, and it seems that kinetics and microstructure evolution are determined by the early grain boundary nucleation microstructure where Type II interfaces are dominant when the nucleation density is high.

Our simulation results indicate that the effects of elastic anisotropy on the kinetics of the displacive transformation become increasingly more significant as the grain boundary nucleation density decreases. It implies that the homogeneous and isotropic elasticity approximation, assumed in all existing phase-field models for the displacive transformations in polycrystals, may not be valid when the grain boundary nucleation density is low for the quantitative predictions although the assumption would be fine for the qualitative predictions.

### **3.4.2. Effects of applied stress**

To explore the effects of applied stress on the phase transformation behaviors in elastically different polycrystals, we also employed the same randomly oriented polycrystals. We chose two different  $\rho$  values, 0.0 and 0.2, because the phase transformations in those two cases are

dominated by different mechanisms due to differences in the grain boundary nucleation density as explained above. The uniaxial stress along  $x$  direction was applied to the polycrystals as the following:

$$\begin{pmatrix} \sigma_{xx}^a & 0 & 0 \\ 0 & 0 & 0 \\ 0 & 0 & 0 \end{pmatrix} \quad (16)$$

where  $\sigma_{xx}^a$  varies from 6.16 MPa ( $\sigma_{xx}^{a*}=0.002$ ) to 61.6 MPa ( $\sigma_{xx}^{a*}=0.02$ ). Fig. 11 shows the microstructures for two different  $\rho$  cases under two selected cases of the applied stress (6.16 MPa and 61.6 MPa) at the later stage (at  $18000\Delta t$ ) and  $\tau_{0.5}$  as a function of applied stress. First of all, the kinetics is more sensitive to the applied stress when the misfit strain is less relaxed at the grain boundaries ( $\rho=0.2$ ) (see the slopes of plots in Fig. 11(b) in comparison with those in Fig. 11(a)). In addition, the differences in the kinetics for different elastic anisotropy are significant for  $\rho=0.2$  for all cases of applied stress magnitudes. In order to investigate the physical origin of the discrepancy in the sensitivity to applied stress, we plotted the von Mises equivalent stress distribution defined in Eq. (15) in the *fcc* random polycrystal under  $\sigma_{xx}^a=61.6$  MPa before the phase transformation occurs. Fig. 12 shows the equivalent stress profiles on the cross sections of the polycrystal shown in Fig. 3(c). As one can see from the figure, the case of isotropic modulus approximation ( $A_z=1.0$ ) displays uniform stress distribution. On the contrary, other anisotropic cases show strongly non-uniform distributions or perturbations of the equivalent stress field. Even if the stress distribution may change as the phase transformation proceeds and the detailed interactions are not clear yet, we speculate that the non-uniform perturbation of the stress field might change the sensitivity to applied stress since it might provide the stress accommodation during the transformation. In addition, the differences in the sensitivity is also attributed to the types of interfaces. When the grain boundary nucleation density is low ( $\rho=0.2$ ), there are more Type I (*bcc/fcc*) interfaces which are more sensitive to the elastic anisotropy. The stress fields arising from the lattice mismatch are coupled to the applied stress in different ways among three different cases of  $A_z$  from the early stage of the transformation. In other words, the elastic anisotropy can be one of major factors that affect the transformation kinetics under the applied stress when the phase transformation is dominated by the phase growth and/or coarsening when

the grain boundary nucleation density is low. However, when grain boundary nucleation density is high ( $\rho=0.0$ ), the effects of elastic anisotropy seem to be minute even though the some minor differences in local microstructures were observed when  $\sigma_{xx}=6.16 \text{ MPa}$  as shown in Fig. 11(a).

It should be mentioned that the plastic deformation under applied stress is not considered in our model and it may change the features of the kinetics under the applied stress when the stress exceeds the yielding stress. It can be studied by employing the model including plasticity such as in [58-60].

#### 4. Summary

We integrated the phase-field equations for displacive transformations in polycrystals and the inhomogeneous elasticity model taking into account the possible misfit strain relaxation at grain boundaries. It was applied to martensitic transformations in the polycrystalline Fe-31at.%Ni alloy as a model system, and systematic computer simulations were carried out to investigate the displacive transformations in polycrystals consisting of elastically anisotropic grains. Our integrated model was able to predict transforming microstructures observed experimentally without explicitly incorporating pre-existing nuclei inside grains or at grain boundaries. It was observed that nucleated variants grow into grains through twin-related structures once two different variants merge or nucleate close to each other. The model also reveals the cooperative nucleation phenomenon across a grain boundary. We examined the effects of grain boundary characteristics including the degree and range of the misfit strain relaxation at the grain boundary and grain boundary curvature on the phase behaviors near the grain boundary employing simple bicrystals containing a flat or curved grain boundary. There exists the optimal misfit strain relaxation for the fastest transformation nucleated at a flat grain boundary. The wider range of the misfit strain relaxation at the grain boundary and the higher curvature of the grain boundary enhance the phase transformation kinetics. The spatial distribution of nucleated phases near the curved grain boundary is completely different from that near the flat grain boundary. Based on the understanding of the phase behaviors near the grain boundary acquired from our computer simulations using the simple bicrystals, we then systematically studied the displacive transformations taking place in realistic polycrystals containing multiple randomly oriented elastically anisotropic grains. The kinetics of the phase transformation was analyzed in terms of

the misfit strain relaxation near grain boundaries and the applied stress. We summarize our three major findings for polycrystals as the followings:

- As the misfit strain becomes more relaxed at grain boundaries, the phase transformation kinetics proceeds faster in general due to the higher grain boundary nucleation density. All the variants nucleate at grain boundaries in generic polycrystals even when the misfit strain is fully relaxed due to the grain boundary curvature in contrast to the case of a bicrystal containing a flat grain boundary.
- As the misfit strain is less relaxed at grain boundaries, *i.e.*, grain boundary nucleation density is low, the kinetics of displacive transformations and the resultant microstructures are more significantly altered by the elastic anisotropy in the polycrystal.
- As the grain boundary nucleation density is low, the kinetics is more sensitive to the applied stress.

To the best of our knowledge, this is the first time to systematically investigate the effect of elastic anisotropy on the displacive transformations in polycrystals using the phase-field approach. It can be utilized for more quantitative simulations of displacive transformations in polycrystals containing elastically anisotropic grains. It should be also emphasized that this model can be combined with our previous work on the phase-field modeling of diffusional processes in elastically inhomogeneous and anisotropic solid solutions [71], rendering the enhanced predictive capability for describing the diffusional-displacive phase transformations [81] in elastically inhomogeneous and anisotropic polycrystals taking place in a variety of materials systems.

## **Acknowledgement**

The work of T.W. Heo was performed under the auspices of the U.S. Department of Energy by Lawrence Livermore National Laboratory (LLNL) under Contract DE-AC52-07NA27344. This work was funded by the Laboratory Directed Research and Development Program at LLNL under project tracking code 12-ERD-053. The work of L.Q. Chen was supported by the Center for Computational Materials Design (CCMD), a joint National Science Foundation (NSF)

Industry/University Cooperative Research Center at Penn State (IIP-1034965) and Georgia Tech (IIP-1034968) and by the National Science Foundation under the grant number DMR-0710483. Helpful discussions with Dr. S. Bhattacharyya (at Indian Institute of Technology Hyderabad), Dr. B.C. Wood (at LLNL), Y.M. Wang (at LLNL), and Mr. Y. An (at LLNL) are acknowledged.

## Figure captions

Fig. 1. Local free energy for displacive transformations: (a) schematic plot of the free energy function, and (b) free energy profiles with different temperatures for Fe-31at.%Ni.

Fig. 2. Tetragonal Bain distortion for the *fcc* to *bcc* transformation (Red arrow direction: contraction, Blue arrow direction: expansion).

Fig. 3. Grain structures generated by phase-field simulations: (a) 2D bicrystal ( $512 \Delta x \times 256 \Delta y$ ), (b) 3D bicrystal ( $256 \Delta x \times 128 \Delta y \times 128 \Delta z$ ), and (c) 3D polycrystal ( $112 \Delta x \times 112 \Delta y \times 112 \Delta z$ ) and its cross section.

Fig. 4. Temporal evolution of *bcc* variants during the grain boundary nucleation process in a 2D bicrystal.

Fig. 5. Temporal evolution of the cooperative nucleation process of *bcc* phases across the grain boundary.

Fig. 6. *Bcc* phase nucleation near a grain boundary with different degrees of misfit strain relaxation at the grain boundary.

Fig. 7. (a) Profiles of  $\phi(\vec{r})$  for different  $\kappa_g$  values and (b) *bcc* phase nucleation near a grain boundary with different ranges of misfit strain relaxation at the grain boundary.

Fig. 8. (a) *Bcc* phase nucleation near a grain boundary with different curvatures of the grain boundary and (b) the magnified view of microstructures with curved grain boundaries at  $5000\Delta t$  in the case of  $A_z=0.5$ .

Fig. 9. (a) Microstructures of the displacive transformations in polycrystals at the later stage (at  $18000\Delta t$ ) for two selected cases of misfit strain relaxation ( $\rho=0.0$  and  $\rho=0.2$ ) with different elastic anisotropy. Total volume fraction ( $V_f$ ) of *bcc* phases as a function of time in a polycrystal with different  $\rho$  values for (b)  $A_z=0.5$ , (c)  $A_z=1.0$ , (d)  $A_z=2.0$ , and (e) required time steps for  $V_f=0.5$  as a function of  $\rho$ .

Fig. 10. (a) Single growing *bcc* variant near a grain boundary in a 2D bicrystal for different cases of elastic anisotropy and (b) corresponding von Mises equivalent stress profiles near the variant.

Fig. 11. Microstructures of the displacive transformations in random polycrystals at the later stage (at  $18000\Delta t$ ) under two selected cases of applied stress and  $\tau_{0.5}$  as a function of applied stress when (a)  $\rho=0.0$  and (b)  $\rho=0.2$ .

Fig. 12. von Mises equivalent stress profiles on the cross sections of polycrystals under  $\sigma_{xx}^a=61.6$  MPa.



## Table

Table 1. Non-dimensionalized parameters

Parameters	Values		
$a_0^*$	0.2		
$a_1^*$	1.8		
$Q^*$	0.1137		
$\kappa_{p,ij,g}^{n*}$	0.02		
$C_{11}^*$	48.5 ( $A_z=0.5$ )	45.5 ( $A_z=1.0$ )	42.4 ( $A_z=2.0$ )
$C_{12}^*$	24.2 ( $A_z=0.5$ )	27.3 ( $A_z=1.0$ )	30.3 ( $A_z=2.0$ )
$C_{44}^*$	6.1 ( $A_z=0.5$ )	9.1 ( $A_z=1.0$ )	12.1 ( $A_z=2.0$ )
$\Delta x^* = \Delta y^* = \Delta z^*$	1.0		
$\Delta t^*$	0.08		

## Reference

- [1] Christian JW, Olson GB, Cohen M. Journal De Physique Iv 1995;5:3.
- [2] Khachaturyan AG. Theory of Structural Transformations in Solids. New York: John Wiley & Sons; 1983.
- [3] Porter DA, Easterling KE. Phase Transformations in Metals and Alloys. 2nd ed. London: Chapman & Hall; 1992.
- [4] Reed-Hill RE, Abbaschian R. Physical Metallurgy Principles. 3rd ed. Boston: PWS Publishing Company; 1994.
- [5] Kingery WD, Bowen HK, Uhlmann DR. Introduction to Ceramics. 2nd ed. New York: John Wiley & Sons; 1976.
- [6] Chiang Y-M, Birnie III DP, Kingery WD. Physical Ceramics. New York: John Wiley & Sons; 1997.
- [7] Lütjering G, Williams JC. Titanium. 2nd ed. Berlin: Springer; 2007.
- [8] Motta AT, Chen LQ. Jom 2012;64:1403.
- [9] Ueda M, Yasuda H, Umakoshi Y. Science and Technology of Advanced Materials 2002;3:171.
- [10] Ueda M, Yasuda HY, Umakoshi Y. Acta Materialia 2003;51:1007.
- [11] Ueland SM, Schuh CA. Journal of Applied Physics 2013;114.
- [12] Wechsler MS, Lieberman DS, Read TA. Transactions of the American Institute of Mining and Metallurgical Engineers 1953;197:1503.
- [13] Bowles JS, Mackenzie JK. Acta Metallurgica 1954;2:129.
- [14] Mackenzie JK, Bowles JS. Acta Metallurgica 1954;2:138.
- [15] Bowles JS, Mackenzie JK. Acta Metallurgica 1954;2:224.
- [16] Bhattacharya K. Acta Metallurgica Et Materialia 1991;39:2431.

- [17] Khachaturyan AG, Shapiro SM, Semenovskaya S. *Physical Review B* 1991;43:10832.
- [18] Li B, Zhang XM, Clapp PC, Rifkin JA. *Journal of Applied Physics* 2004;95:1698.
- [19] Denoual C, Caucci AM, Soulard L, Pellegrini YP. *Physical Review Letters* 2010;105.
- [20] Chen LQ. *Annual Review of Materials Research* 2002;32:113.
- [21] Boettinger WJ, Warren JA, Beckermann C, Karma A. *Annu Rev Mater Res* 2002;32:163.
- [22] Granasy L, Pusztai T, Börzsönyi T, Toth G, Tegze G, Warren JA, Douglas JF. *J Mater Res* 2006;21:309.
- [23] Emmerich H. *Adv Phys* 2008;57:1.
- [24] Moelans N, Blanpain B, Wollants P. *Comput Coupling Phase Diagr Thermochem* 2008;32:268.
- [25] Steinbach I. *Modelling Simul Mater Sci Eng* 2009;17:073001.
- [26] Cahn JW, Hilliard JE. *J Chem Phys* 1958;28:258.
- [27] Wang Y, Khachaturyan AG. *Acta Mater* 1997;45:759.
- [28] Artemev A, Jin Y, Khachaturyan AG. *Acta Mater* 2001;49:1165.
- [29] Wen YH, Wang Y, Chen LQ. *Acta Materialia* 1999;47:4375.
- [30] Wen YH, Wang Y, Chen Q. *Philosophical Magazine a-Physics of Condensed Matter Structure Defects and Mechanical Properties* 2000;80:1967.
- [31] Wen YH, Wang Y, Bendersky LA, Chen LQ. *Acta Materialia* 2000;48:4125.
- [32] Wen YH, Chen LQ, Hazzledine PM, Wang Y. *Acta Materialia* 2001;49:2341.
- [33] Wen YH, Wang Y, Chen LQ. *Acta Materialia* 2001;49:13.
- [34] Wen YH, Wang Y, Chen LQ. *Acta Materialia* 2002;50:13.
- [35] Bhattacharyya S, Abinandanan TA. *Acta Materialia* 2009;57:646.
- [36] Mamivand M, Zaeem MA, El Kadiri H, Chen LQ. *Acta Materialia* 2013;61:5223.
- [37] Kundin J, Emmerich H, Zimmer J. *Philosophical Magazine* 2010;90:1495.
- [38] Kundin J, Raabe D, Emmerich H. *Journal of the Mechanics and Physics of Solids* 2011;59:2082.
- [39] Guo XH, Shi SQ, Ma XQ. *Applied Physics Letters* 2005;87.
- [40] Yeddu HK, Borgenstam A, Hedstrom P, Agren J. *Materials Science and Engineering a-Structural Materials Properties Microstructure and Processing* 2012;538:173.
- [41] Yeddu HK, Malik A, Agren J, Amberg G, Borgenstam A. *Acta Materialia* 2012;60:1538.
- [42] Yeddu HK, Razumovskiy VI, Borgenstam A, Korzhavyi PA, Ruban AV, Agren J. *Acta Materialia* 2012;60:6508.
- [43] Yeddu HK, Borgenstam A, Agren J. *Acta Materialia* 2013;61:2595.
- [44] Yeddu HK, Lookman T, Saxena A. *Acta Materialia* 2013;61:6972.
- [45] Yamanaka A, Takaki T, Tomita Y. *International Journal of Mechanical Sciences* 2010;52:245.
- [46] Rao W-F, Khachaturyan AG. *Acta Mater* 2011;59:4494.
- [47] Zhang W, Jin YM, Khachaturyan AG. *Acta Materialia* 2007;55:565.
- [48] Gao Y, Zhou N, Yang F, Cui Y, Kovarik L, Hatcher N, Noebe R, Mills MJ, Wang Y. *Acta Materialia* 2012;60:1514.
- [49] Wang YU, Jin YM, Khachaturyan AG. *Acta Mater* 2004;52:1039.
- [50] She H, Liu YL, Wang BA. *International Journal of Solids and Structures* 2013;50:1187.
- [51] Seol DJ, Hu SY, Li YL, Chen LQ, Oh KH. *Materials Science Forum* 2002;408-412:1645.
- [52] Seol DJ, Hu SY, Li YL, Chen LQ, Oh KH. *Metals and Materials International* 2003;9:221.
- [53] Artemev A, Wang Y, Khachaturyan AG. *Acta Mater* 2000;48:2503.
- [54] Wang YZ, Khachaturyan AG. *Materials Science and Engineering a-Structural Materials Properties Microstructure and Processing* 2006;438:55.
- [55] Mamivand M, Zaeem MA, El Kadiri H. *Computational Materials Science* 2013;77:304.
- [56] Jin YM, Artemev A, Khachaturyan AG. *Acta Mater* 2001;49:2309.
- [57] Artemev A, Jin Y, Khachaturyan AG. *Phil Mag A* 2002;82:1249.
- [58] Malik A, Yeddu HK, Amberg G, Borgenstam A, Agren J. *Materials Science and Engineering a-Structural Materials Properties Microstructure and Processing* 2012;556:221.
- [59] Malik A, Amberg G, Borgenstam A, Agren J. *Acta Materialia* 2013;61:7868.

- [60] Malik A, Amberg G, Borgenstam A, Agren J. Modelling and Simulation in Materials Science and Engineering 2013;21:85003.
- [61] Bhattacharyya S, Heo TW, Chang K, Chen L-Q. Modelling Simul Mater Sci Eng 2011;19:035002.
- [62] Bhattacharyya S, Heo TW, Chang K, Chen L-Q. Commun Comput Phys 2012;11:726.
- [63] Tang M, Carter WC, Cannon RM. Phys Rev B 2006;73.
- [64] Tang M, Carter WC, Cannon RM. J Mater Sci 2006;41:7691.
- [65] Jang D, Atzmon M. J Appl Phys 2006;99.
- [66] Tang M, Carter WC, Cannon RM. Phys Rev Lett 2006;97.
- [67] Sutton AP, Balluffi RW. Interfaces in Crystalline Materials. New York: Oxford University Press Inc.; 1995.
- [68] Pozdnyakov VA. Dokl Phys 2007;52:24.
- [69] Hu SY, Chen L-Q. Acta Mater 2001;49:1879.
- [70] Yu P, Hu SY, Chen L-Q, Du Q. J Comp Phys 2005;208:34.
- [71] Heo TW, Bhattacharyya S, Chen LQ. Philosophical Magazine 2013;93:1468.
- [72] Chen L-Q, Yang W. Phys Rev B 1994;50:15752.
- [73] Krill III CE, Chen L-Q. Acta Mater 2002;50:3057.
- [74] Vinnikov LY, Georgieva IY, Maistrenko LG, Mogutnov BM, Polovov VM. Metallofizika 1974;24.
- [75] Kaufman L, Cohen M. Transactions of the American Institute of Mining and Metallurgical Engineers 1956;206:1393.
- [76] Zhu L-H, Huang Q-W. Materials Letters 2003;57:4070.
- [77] Breedis JF, Wayman CM. Transactions of the Metallurgical Society of Aime 1962;224:1128.
- [78] Hausch G. Acta Metallurgica 1973;21:401.
- [79] Schmidt I, Gross D. Journal of the Mechanics and Physics of Solids 1997;45:1521.
- [80] Raabe D, Sandlobes S, Millan J, Ponge D, Assadi H, Herbig M, Choi PP. Acta Materialia 2013;61:6132.
- [81] Christian JW. Metallurgical and Materials Transactions a-Physical Metallurgy and Materials Science 1994;25:1821.

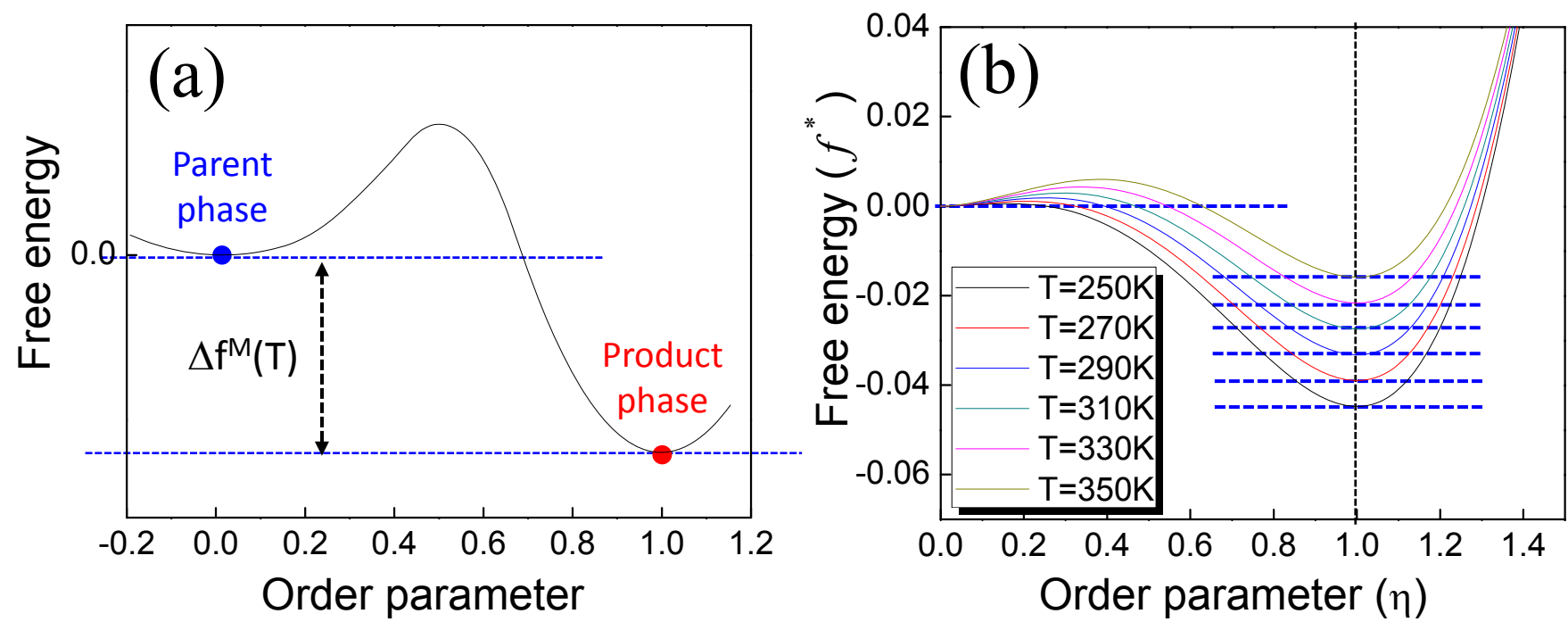


Fig. 1

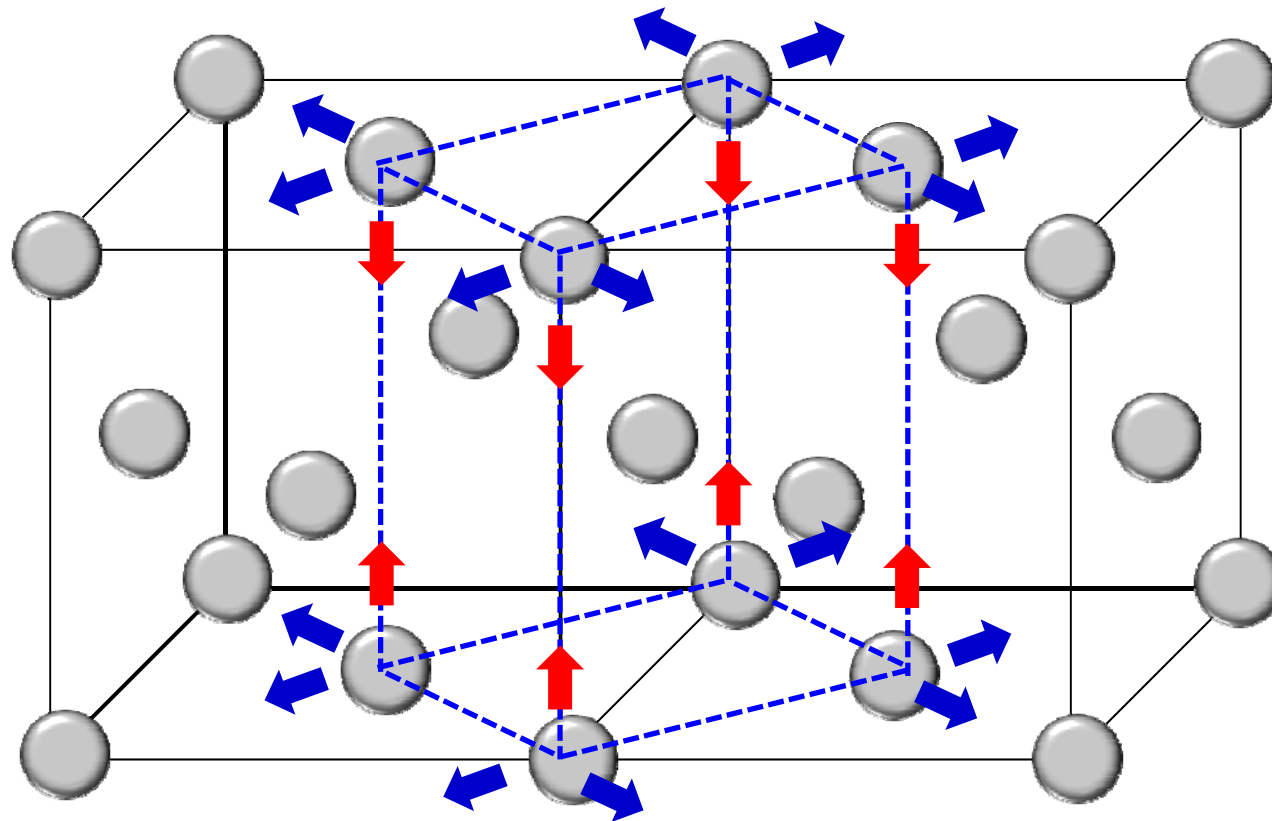


Fig. 2

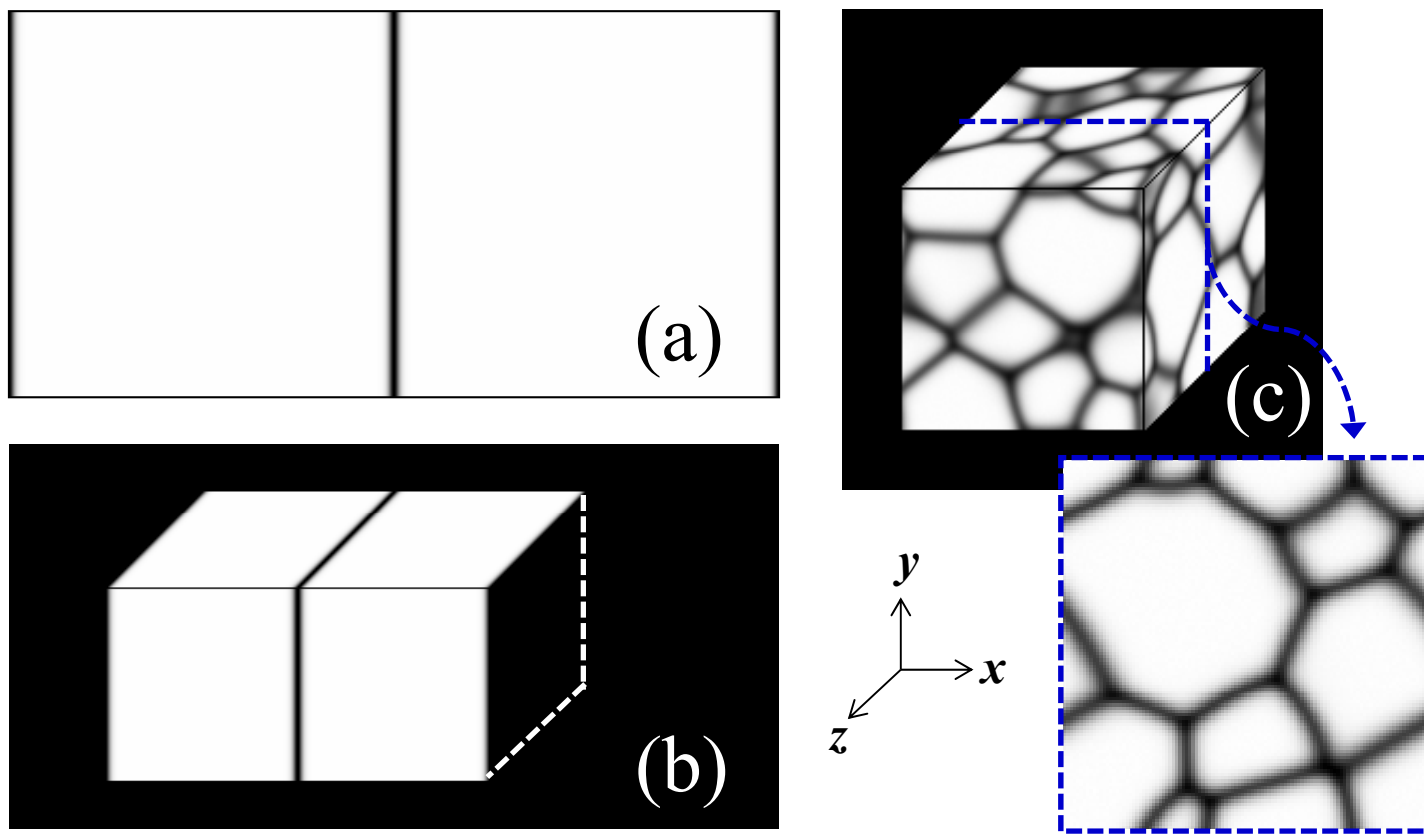


Fig. 3

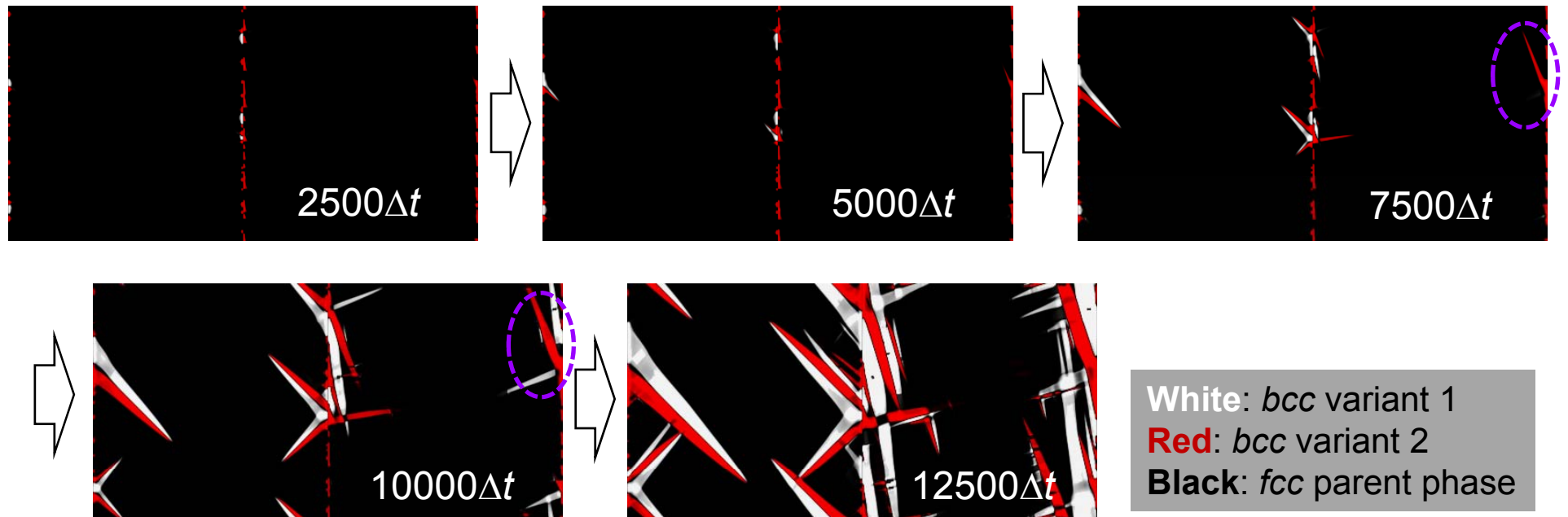


Fig. 4

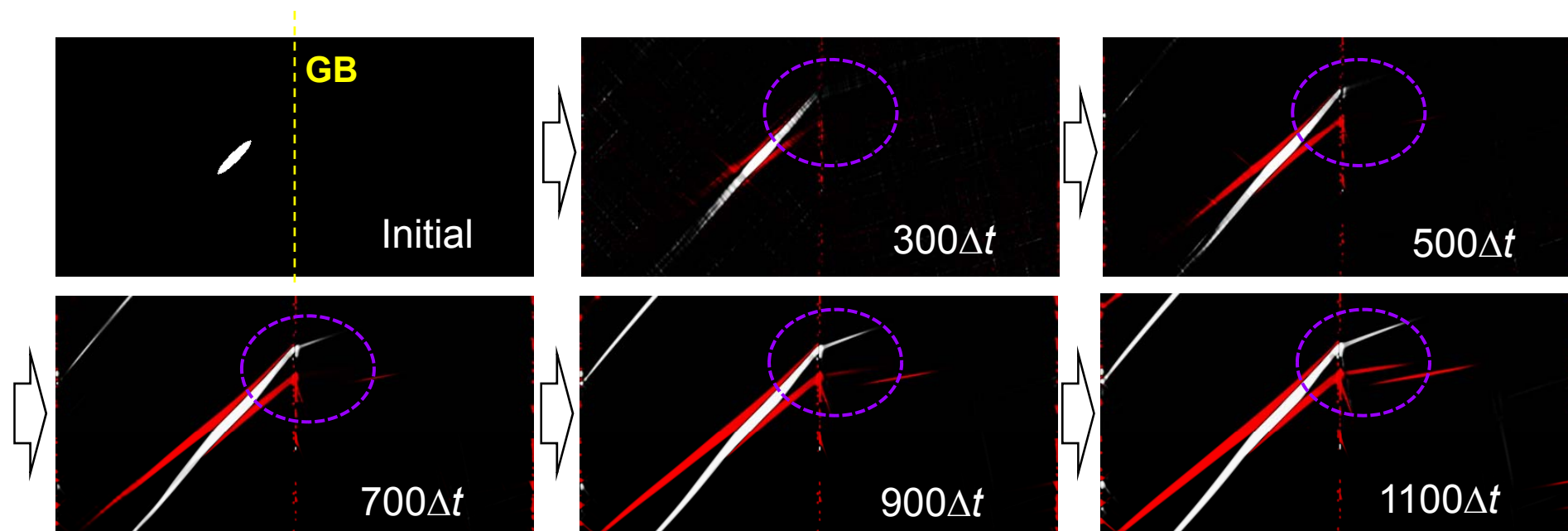


Fig. 5



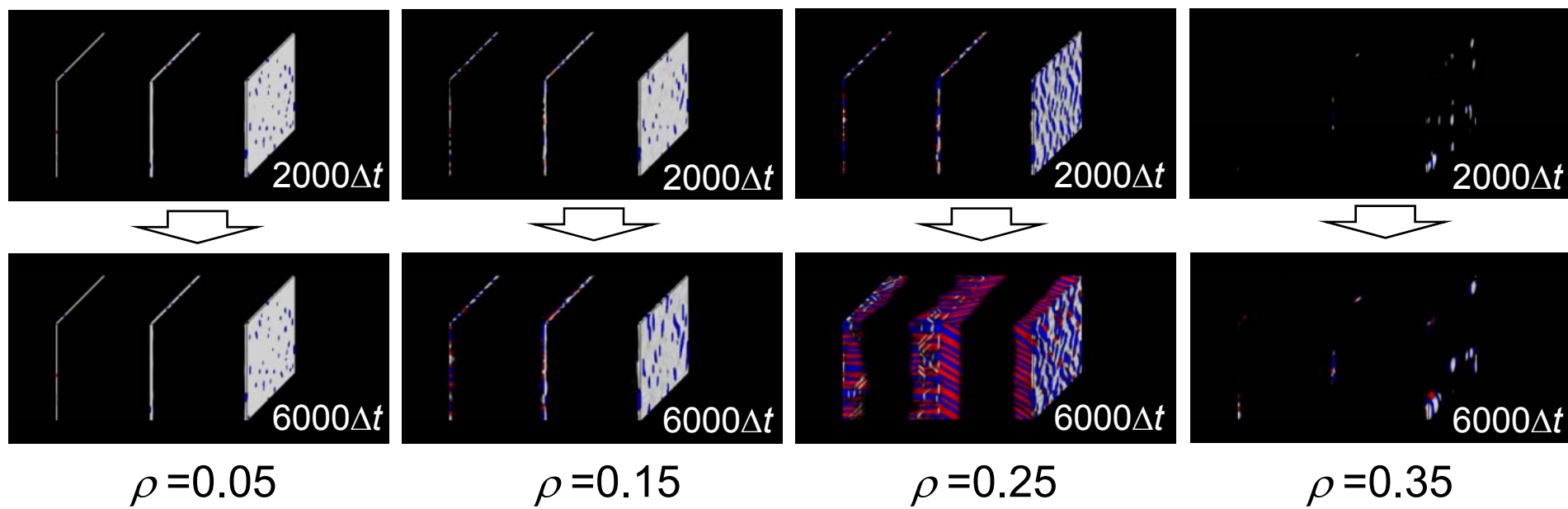
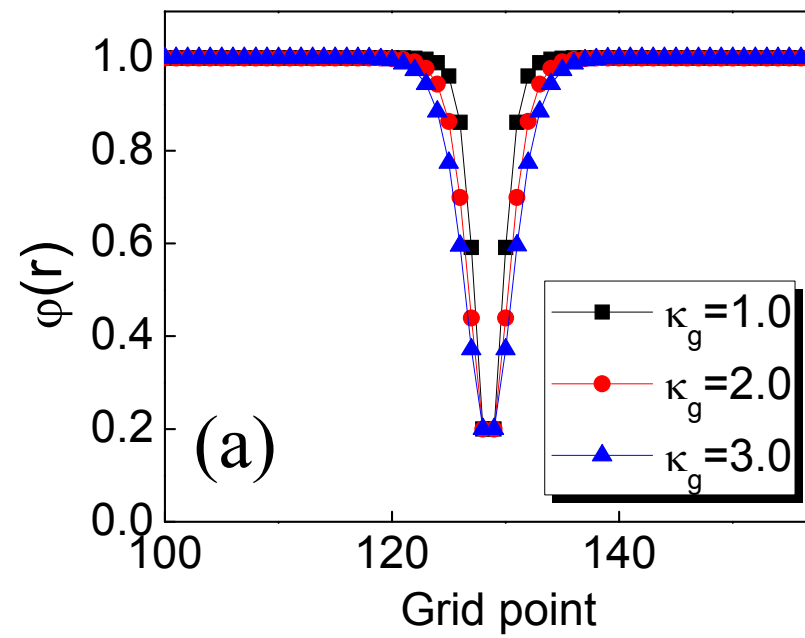


Fig. 6



(b)

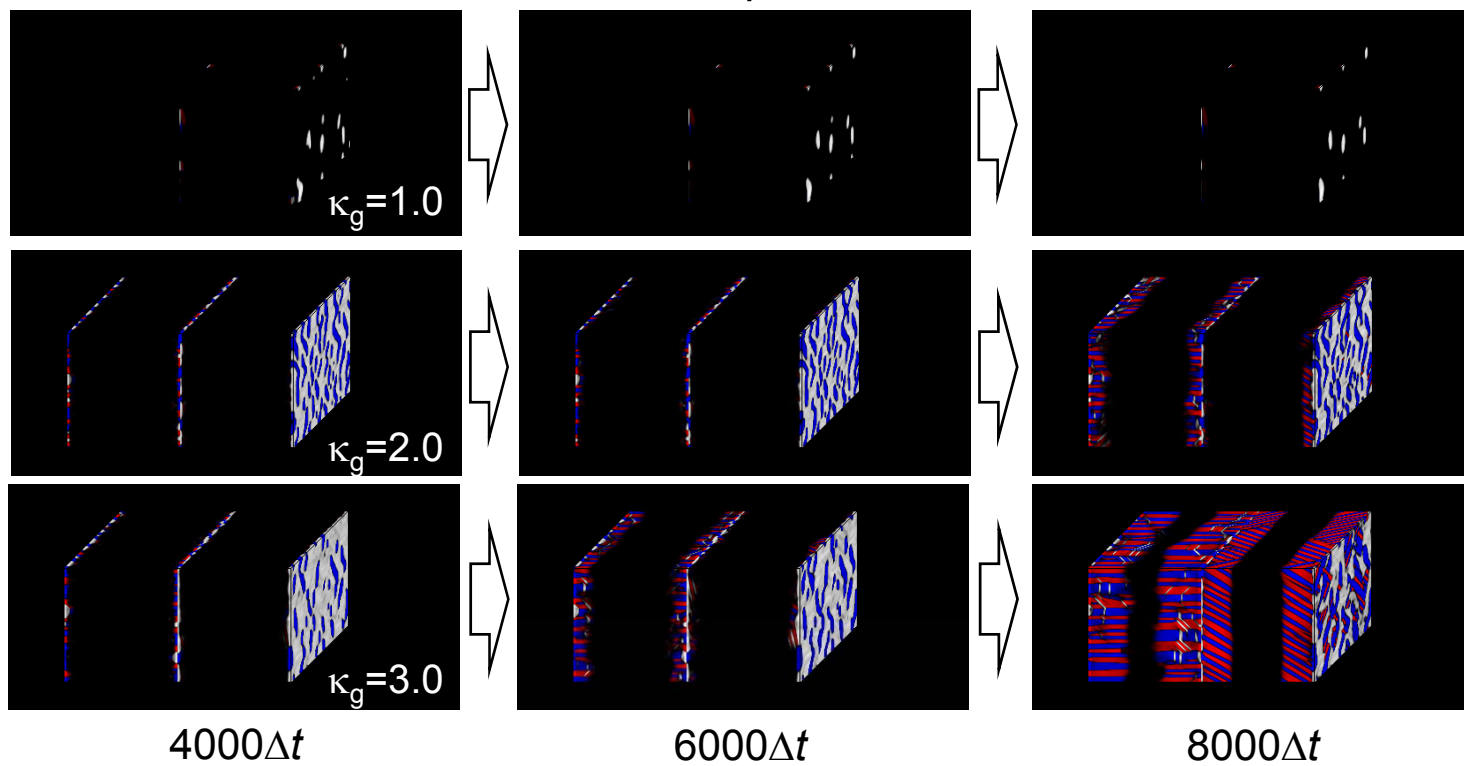
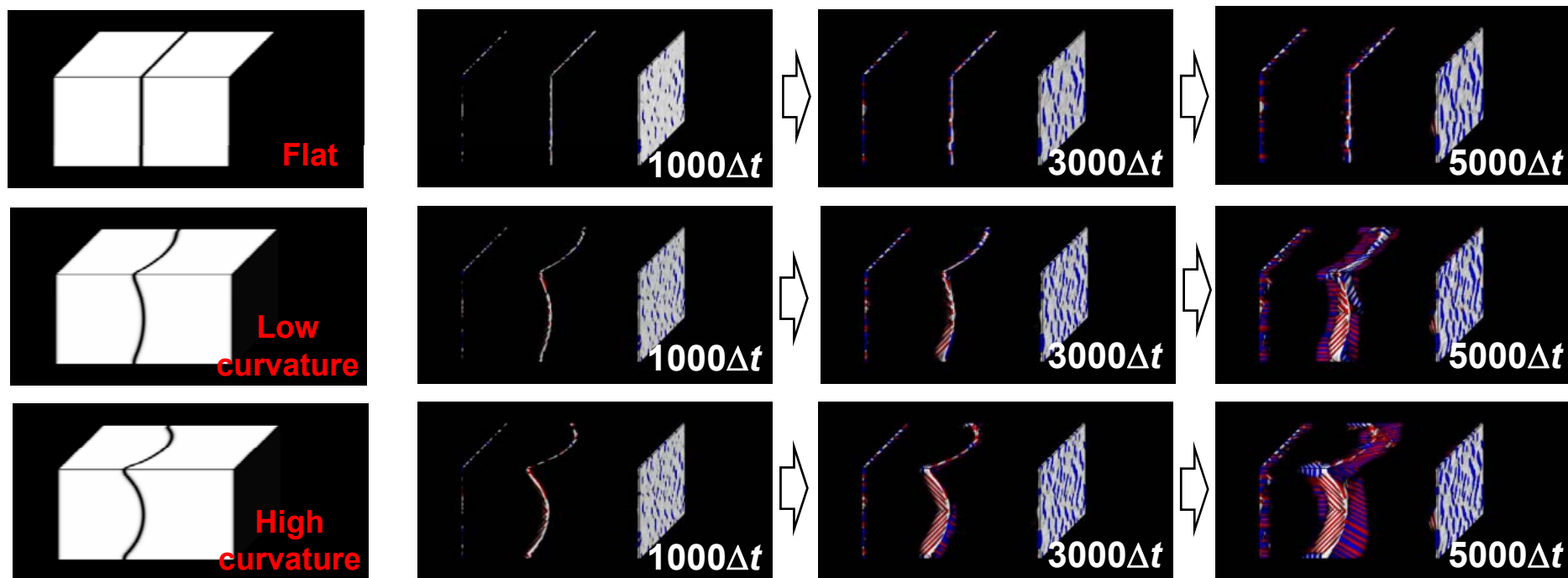
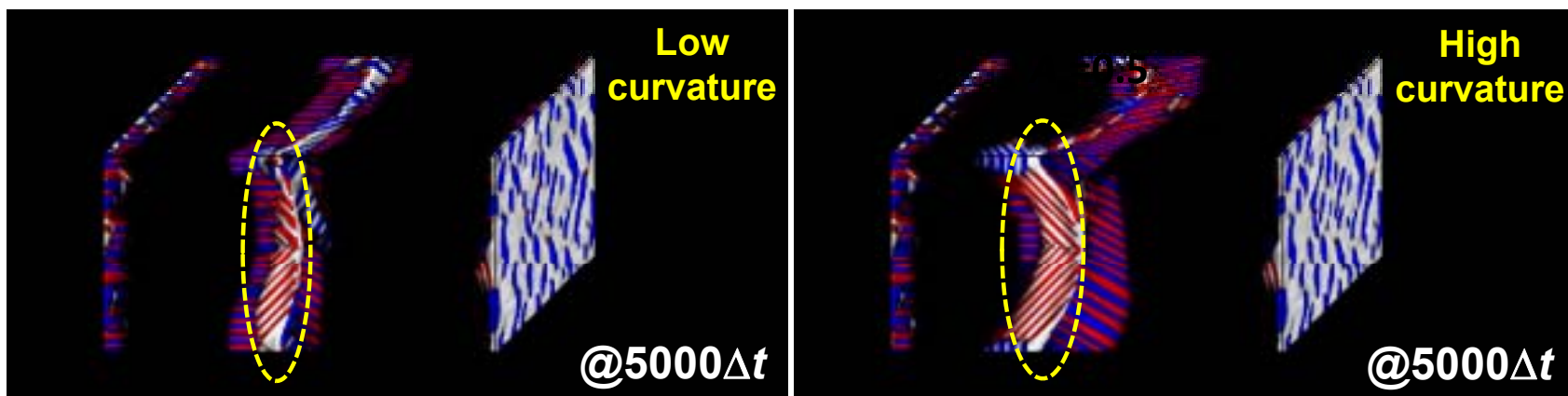


Fig. 7



(a)



(b)

White: *bcc* variant 1  
 Red: *bcc* variant 2  
 Blue: *bcc* variant 3  
 Black: *fcc* parent phase

Fig. 8

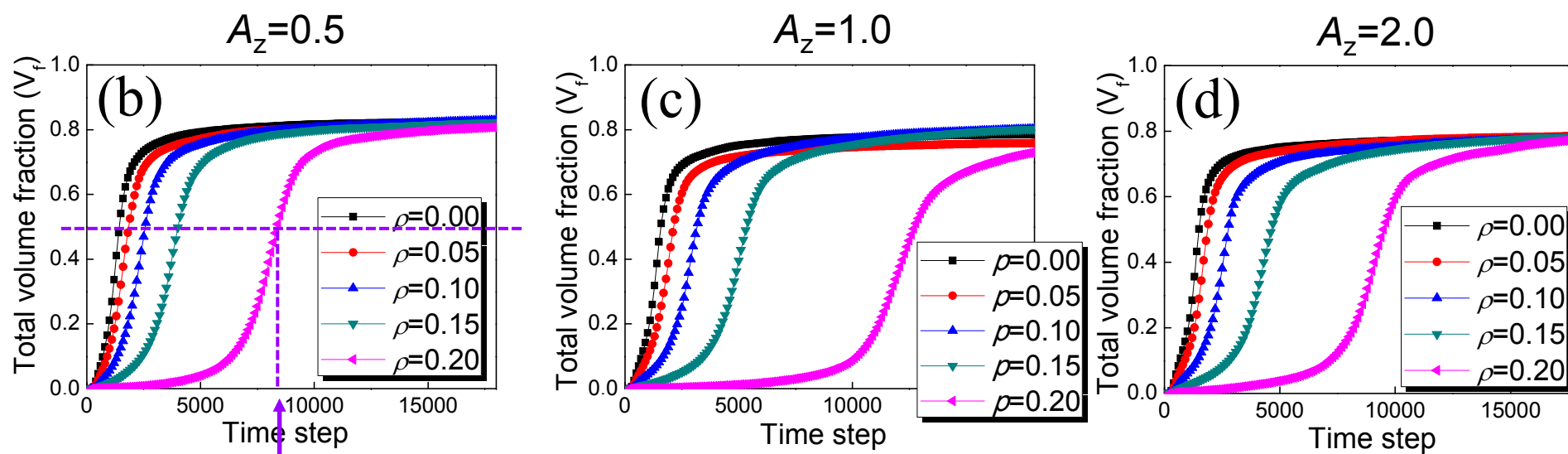
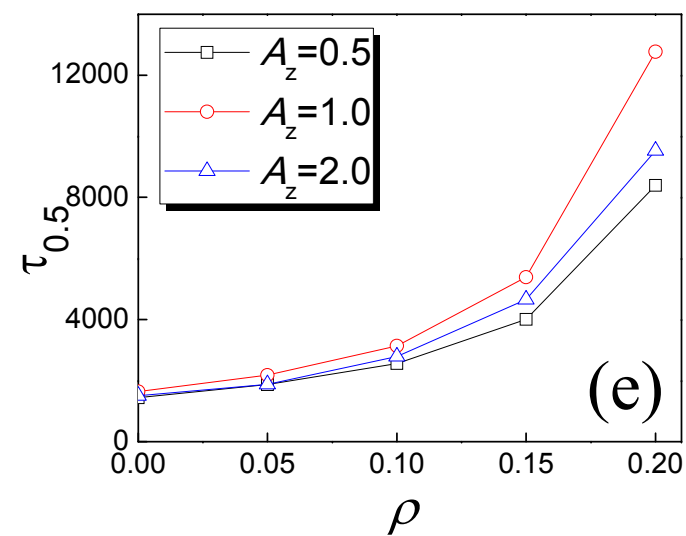
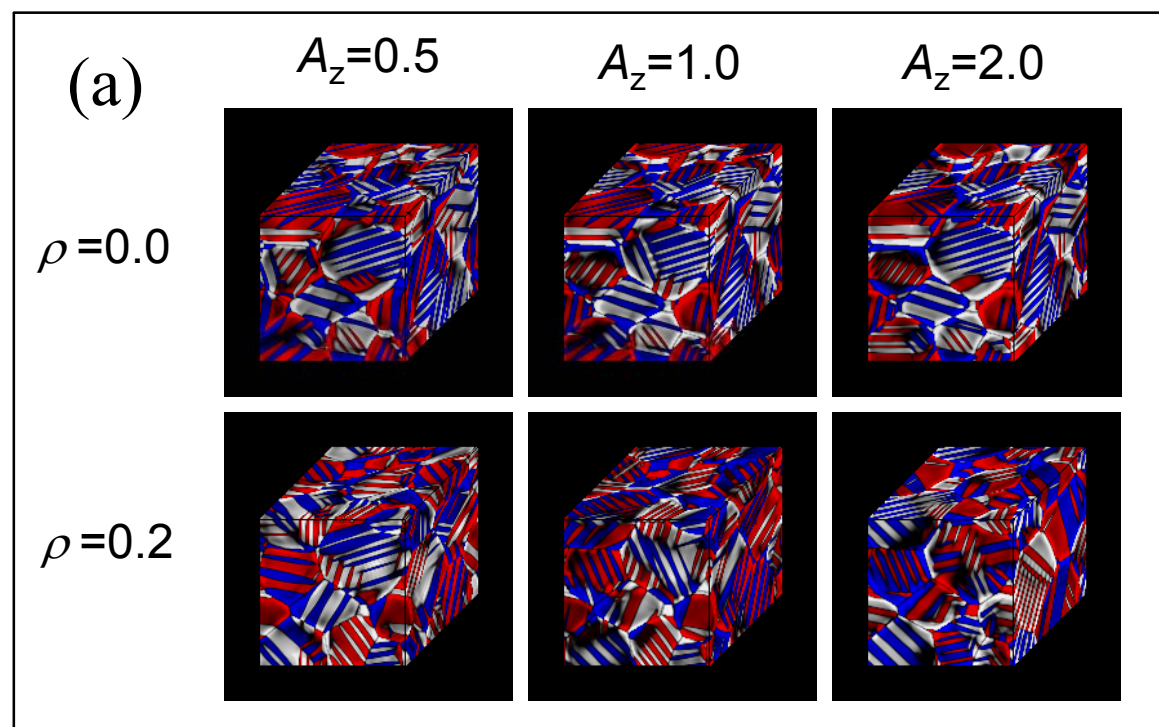


Fig. 9

$\tau_{0.5}$

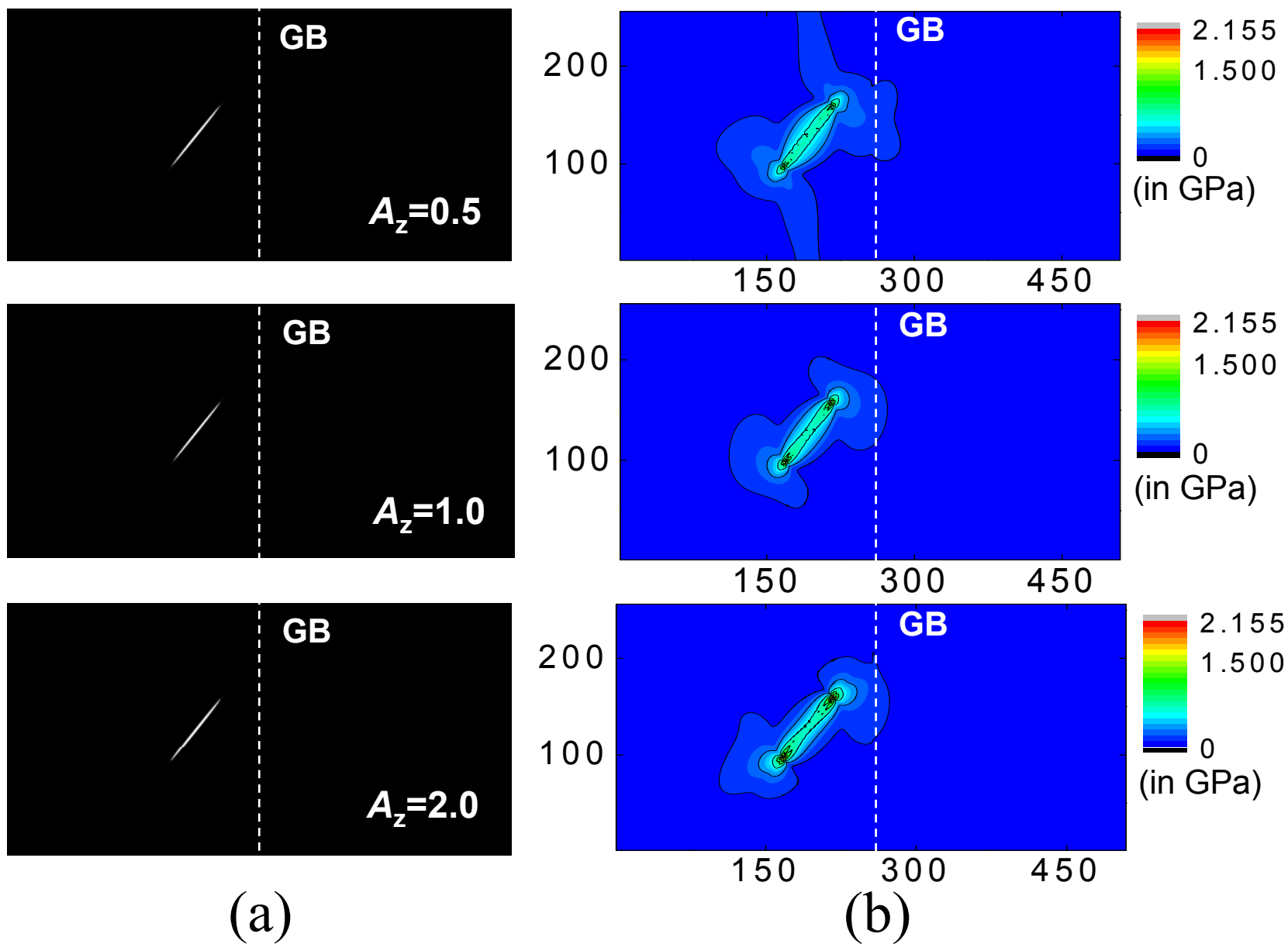


Fig. 10

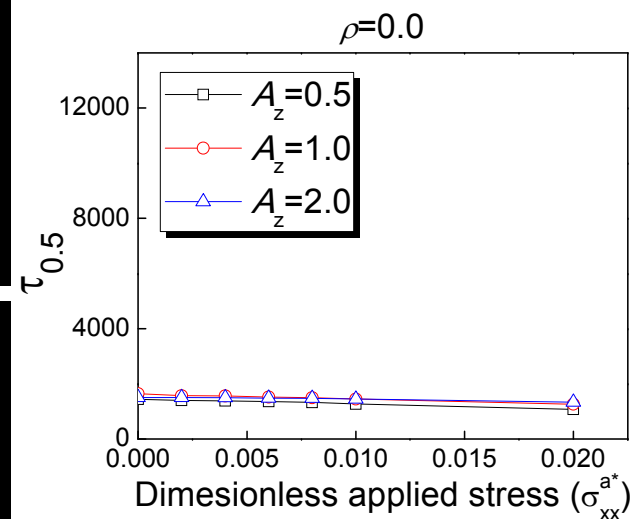
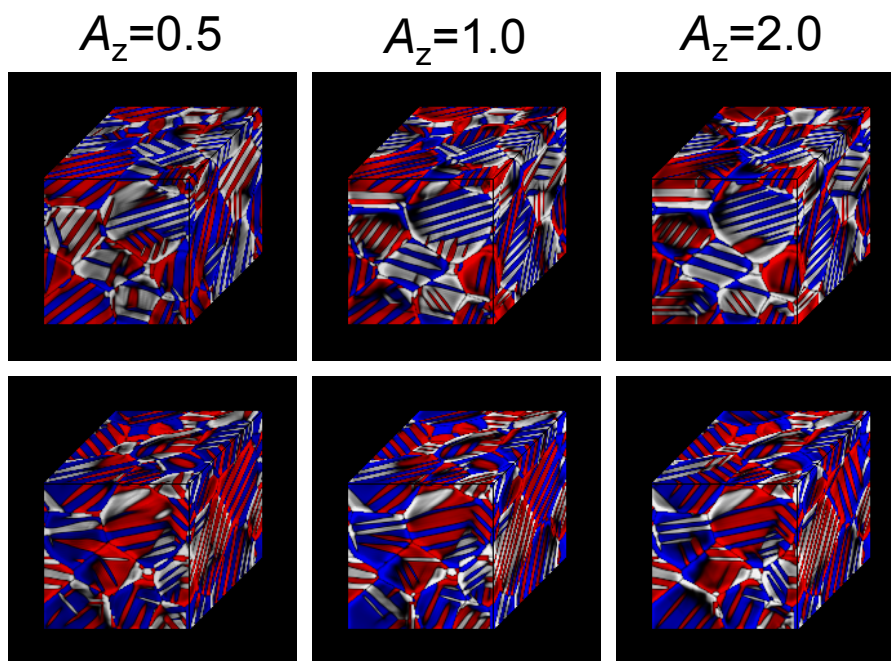
(a)  $\rho=0.0$

$$\sigma_{xx}^a = 6.16 \text{ MPa}$$

$$(\sigma_{xx}^{a*} = 0.002)$$

$$\sigma_{xx}^a = 61.6 \text{ MPa}$$

$$(\sigma_{xx}^{a*} = 0.02)$$



(b)  $\rho=0.2$

$$\sigma_{xx}^a = 6.16 \text{ MPa}$$

$$(\sigma_{xx}^{a*} = 0.002)$$

$$\sigma_{xx}^a = 61.6 \text{ MPa}$$

$$(\sigma_{xx}^{a*} = 0.02)$$

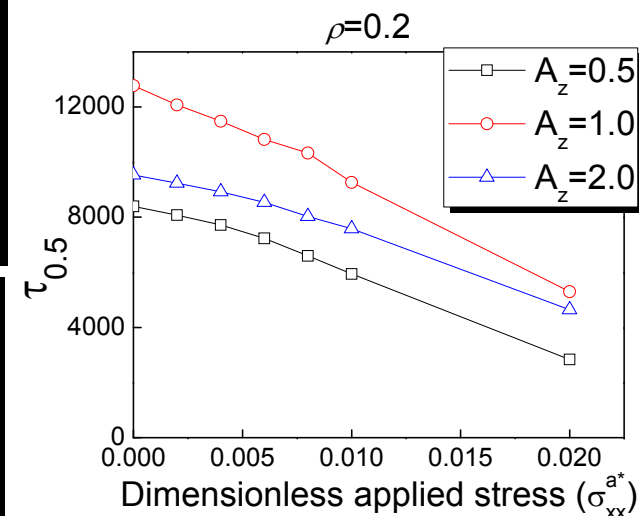
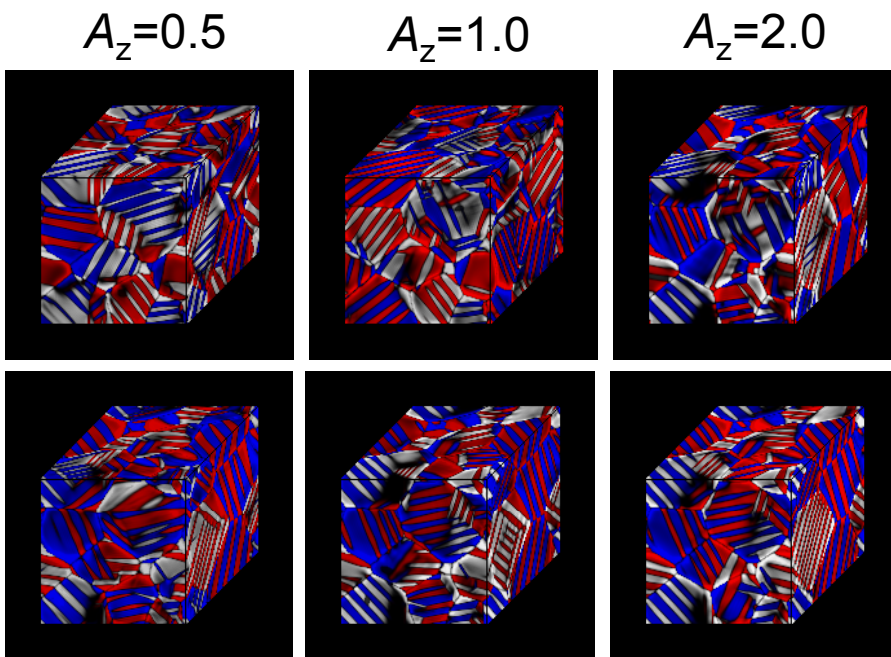


Fig. 11

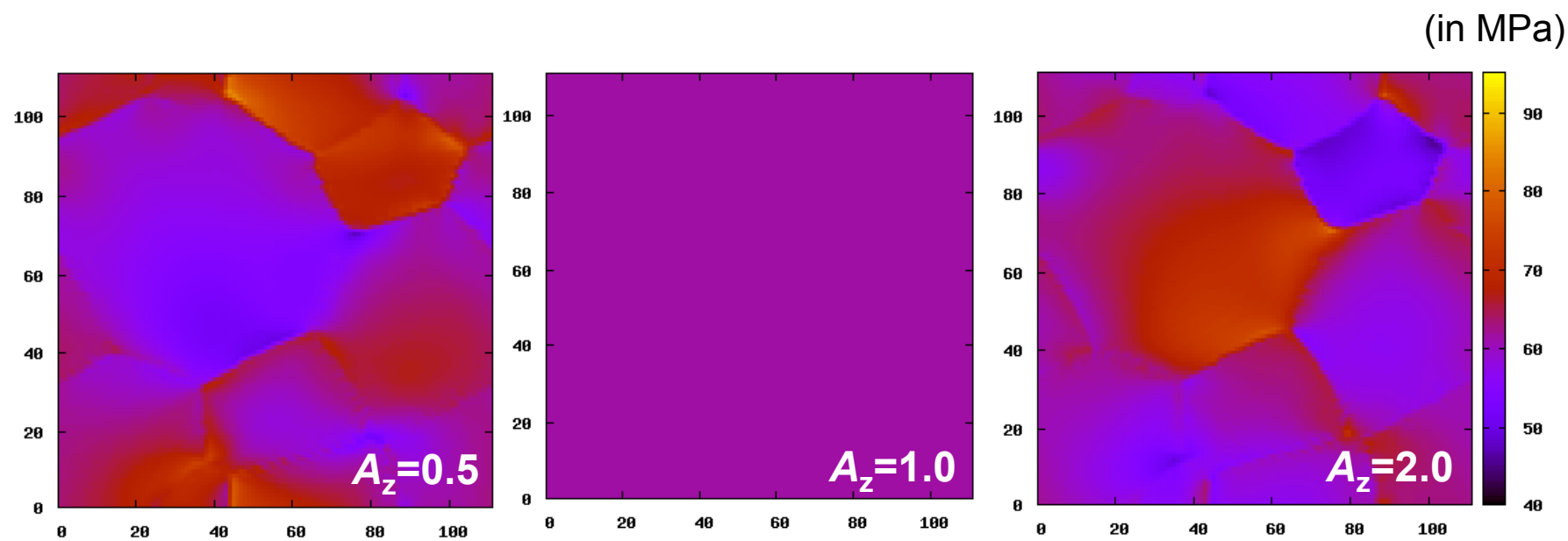


Fig. 12



**Supplementary Materials**  
**To**  
**Phase-field Modeling of Displacive Phase Transformations in Elastically**  
**Anisotropic and Inhomogeneous Polycrystals**

**Tae Wook Heo<sup>1,\*</sup> and Long-Qing Chen<sup>2</sup>**

<sup>1</sup>*Condensed Matter and Materials Division, Lawrence Livermore National Laboratory, Livermore, CA 94550, USA*

<sup>2</sup>*Department of Materials Science and Engineering, The Pennsylvania State University, University Park, PA 16802, USA*

\*E-mail address: heo1@llnl.gov, htww584@gmail.com

**S1. Computational efficiency of the developed model**

To check the computational efficiency of the explained scheme in section 2.3, we measured the simulation time of the displacive transformation simulations for the same amount of time steps ( $15000 \Delta t$ ) using the several cases of 3D grain structures ( $112 \Delta x \times 112 \Delta y \times 112 \Delta z$ ) consisting of different numbers ( $g$ ) of grain order parameters ( $\xi_g$ ). The simulations were performed using the parallel computers (112 processors) and the measured simulation time for the given cases normalized by the simulation time of the case where  $g=1$  (single crystal) for comparison is tabulated in Table S.1. In order to look into the computational efficiency of the scheme in section 2.3 itself, let us take a look at the results in the case of isotropic elasticity where no iterations for the elastic solutions are required. As one can see from the table, there is no significant simulation time increase although the number of grain order parameters increases. The loss of the efficiency might be mainly attributed to the computation of the variational derivative of the gradient energy term ( $\kappa_{p,ij,g} \nabla_i \nabla_j \eta_{pg}$ ) in the Fourier space since all the structural order parameters should be considered at all grid points for this computation. With regard to the computational efficiency associated with the inhomogeneous elasticity, the computer simulations with the inhomogeneous elasticity requires approximately 1.5 times longer simulation time as shown in Table S.1 compared to those with the homogeneous elasticity due to the iterations for



the accurate elastic solutions as explained in section 2.2. In other words, employing the inhomogeneous elasticity does not require a significant increase in computational time.

Table S.1. Simulation time of 3D computer simulations of the displacive transformation

# of $\xi_g$	Normalized simulation time* (Homogeneous elasticity)	Normalized simulation time* (Inhomogeneous elasticity)
1	1	-
8	1.86	2.86
12	2.44	3.97
17	3.15	4.47

\*Normalized by the simulation time of  $g=1$

## S2. Grain structure generation

For a grain structure containing multiple grains, a set of grain order parameters ( $\xi_g$ ) are employed. The final grain structures are prepared by solving the following Allen-Cahn equation:

$$\frac{\partial \xi_g(\vec{r}, t)}{\partial t} = -L_g \left( \frac{\partial f_g(\{\xi_g\})}{\partial \xi_g} - \kappa_g \nabla^2 \xi_g \right), \quad (\text{S.1})$$

where  $L_g$  is the kinetic coefficient related to grain boundary mobility,  $\kappa_g$  is the gradient energy coefficient for grain order parameters, and  $f_g$  is the free energy density function of grain order parameters given by  $f_g(\{\xi_g\}) = \sum_g \left( -\frac{1}{2} \xi_g^2 + \frac{1}{4} \xi_g^4 \right) + \gamma \sum_g \sum_{g' > g} \xi_g^2 \xi_{g'}^2$ , with the phenomenological parameter ( $\gamma$ ) for the interactions among grain order parameters. The equations are solved by semi-implicit Fourier-spectral method [1].

## S3. 3D computer simulation of *bcc* variants nucleation at grain boundaries

A 3D computer simulation was conducted with  $T=205K$ ,  $A_z=0.5$ , and  $\rho=0.2$  to check if the nucleation of *bcc* variants occurs by the same mechanism. The Euler angles of the left-hand and right hand side grains were set to be (0,0,0) and  $(\pi/6, 0, 0)$ , respectively. Fig. S.1 shows the

evolution of grain boundary nucleated *bcc* variants in the 3D system and the snapshots of a cross section during the nucleation stage of a displacive transformation near a grain boundary. As shown in the figure, when two different variants are in contact, they propagate to the grain interior as in the 2D simulation in section 3.2.

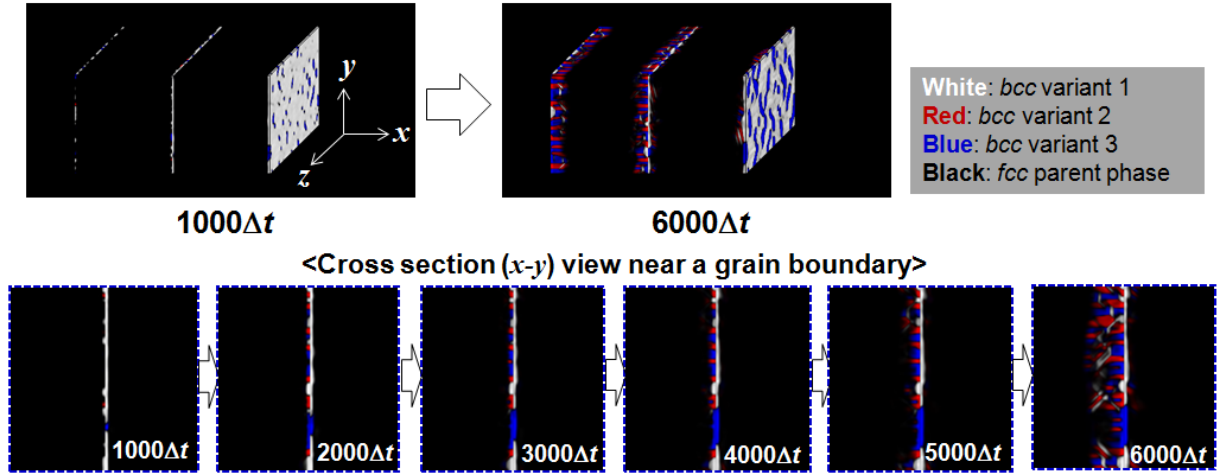


Fig. S.1. Temporal evolution of *bcc* variants during the grain boundary nucleation process in a 3D bicrystal.

#### S4. Temporal evolution of the displacive transformation in polycrystals

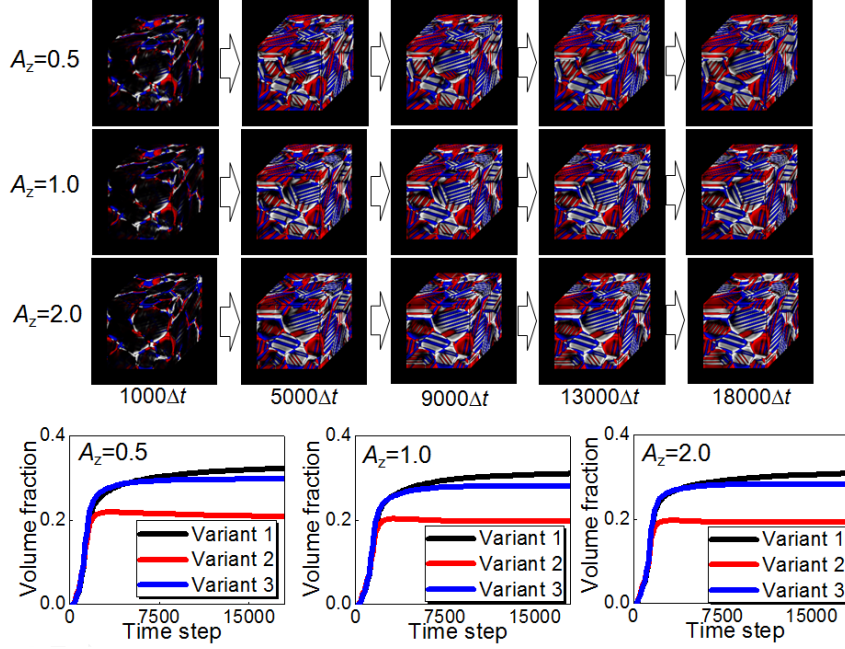


Fig. S.2. Temporal evolution of the displacive transformation in polycrystals for  $\rho = 0.0$  for different elastic anisotropy cases and the volume fraction of each variant as a function of time.

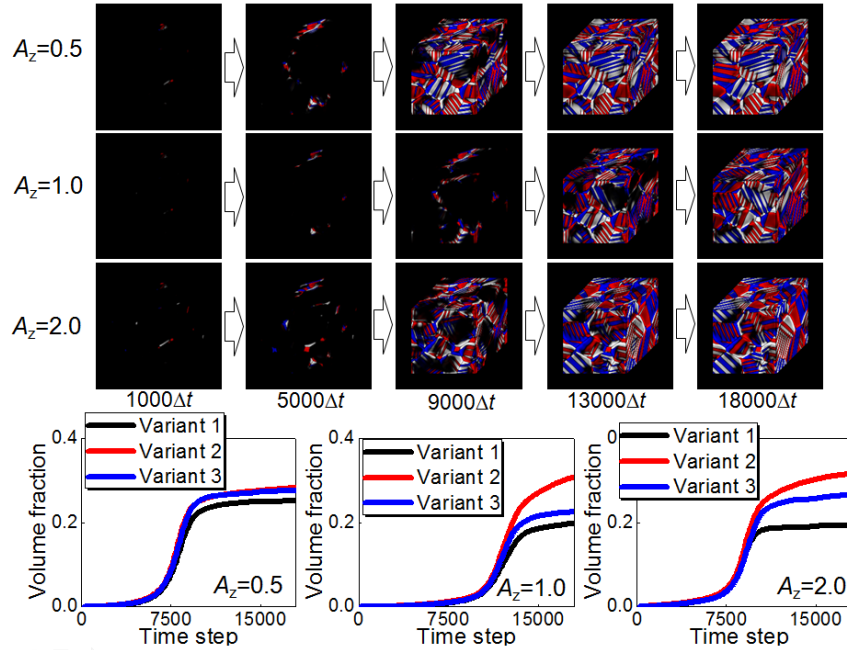


Fig. S.3. Temporal evolution of the displacive transformation in polycrystals for  $\rho = 0.2$  for different elastic anisotropy cases and the volume fraction of each variant as a function of time.

## References

- [1] Chen L-Q, Shen J. Comp Phys Comm 1998;108:147.